Wageningen University
Meteorology and Air Quality Group

Master Thesis

Shallow Drainage Flows over Light Sloping Terrain during BLLAST 2011: Two Case Studies

Author:
Lisanne Nauta

Supervisor:
Dr.Ir. Oscar Hartogensis

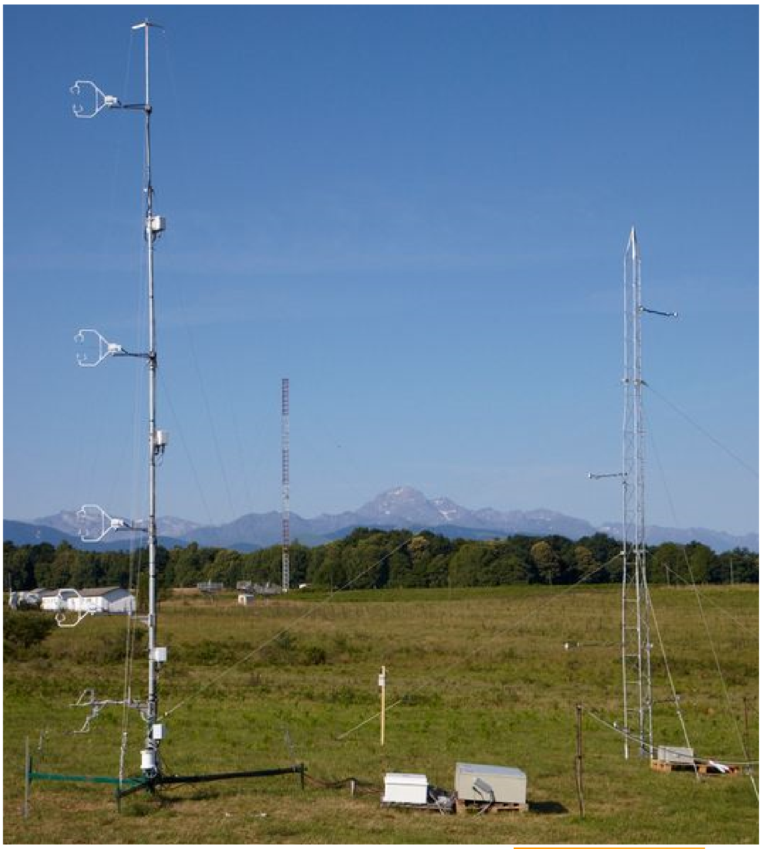

December 5, 2013

Abstract

In this thesis, we emphasize on the submeso motion called "shallow drainage flow" by doing case studies. More physical understanding of submeso motions from field experiments is still needed for modelling purposes. A dense network of eddy covariance (EC) and thermocouple data is used from the BLLAST 2011 campaign in Lannemezan (France). Two suitable cases (IOP 3+4) with shallow drainage flow within 10m are selected from 5min averaged vertical profiles. Studying fine scales in extreme stable conditions by ordinary wavelet analysis is hard due to the mixture of scales and non-stationary intermittent turbulence. Therefore, a new spectral analysis technique is developed that combines the benefits of both ogives and wavelets. Using this technique, we can to some extent eliminate the unwanted larger scale effects. From results, it appeared to be a promising tool to determine averaging time scale for turbulent fluxes.

Results show that the arrival of shallow drainage flow is typically just after the early evening calm period when the turbulent kinetic energy was almost zero. We demonstrate that the flow is characterized by a wavelike evolution, cold micro-fronts and shifting wind directions by time series analysis. Moreover, shear instability appeared to be the main drive of turbulent mixing within 1m. Near surface warming till 3°C and surface temperature increase till 1°C was measured due to turbulent mixing event induced by shallow drainage flow. Thermal IR photos appeared to be useful and showed that the oscillating surface temperature varies in space, which was not earlier showed. TKE budgets, however, did not contribute to more physical understanding due to very low fluxes and EC instruments outside the range of near surface mixing. Finally, all results are combined to sketch a conceptual model of the flow.

Contents

Chapter 1

Introduction

1.1 Theory and Background

This thesis will concentrate on the description of typical near surface motions during extreme stable conditions in the stable boundary layer (SBL). We focus on shallow drainage flows in particular, which occur when cold air accelerates along a slope. Observational data from the Boundary Layer Late Afternoon and Sunset Turbulence (BLLAST) campaign is used for this study, where the emphasis is on the physical understanding of these typical motions by doing case studies.

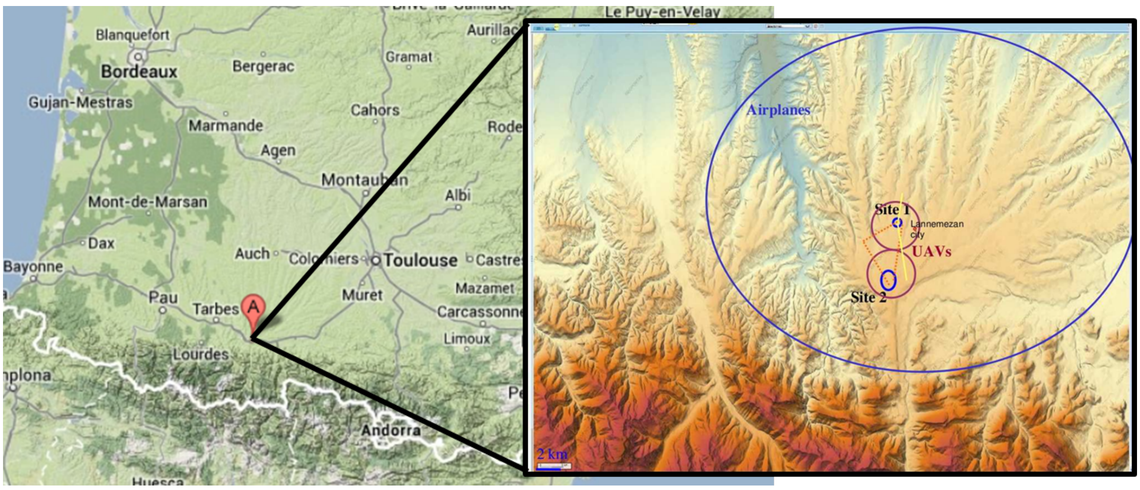

Figure 1.1: Right: The location of the BLLAST campaign in Lannemezan in the South of France idicated by A. Left: A zoomed in figure of the topography of the BLLAST monitoring sites and surroundings.

The BLLAST experiment was an extensive measurement campaign in Lannemezan (France) organised by various international groups from 14 June to 8 July 2011. The measurement area is located close to the mountain feet of the Pyrenees and divided in multiple monitoring sites as represented in figure 1.1. A 10m tower equipped with 6 eddy covariance (EC) sonics and additional thermocouples even below 50 cm located at super site 1 plays a central role in this study. Under low synoptic conditions, the influence of the surrounding topography is very important in this study. More details about the measurement site and instrumentation is given in section 2.

The SBL is part of the atmospheric boundary layer (ABL), which is the bottom layer of the atmosphere that is directly influenced by the earth's surface. The structure of the ABL evolves with the diurnal cycle according to figure 1.2, where the mixed layer (ML), residual layer and SBL are the most important components (Stull, 1988). Around sunset, the surface starts to cool due to radiative cooling and heat is extracted from the air. Air parcels become negatively buoyant and the colder and heavier air sinks, which forms a stably stratified layer. In the SBL, turbulence is suppressed by stratification and can only be generated by wind shear.

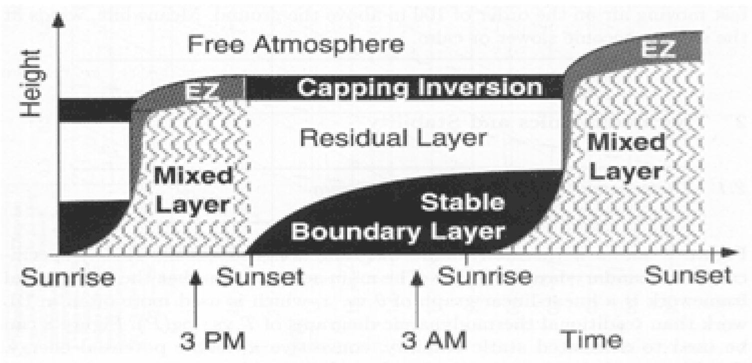

Figure 1.2: Time evolution the atmospheric boundary layer structure. From Stull (1988)

The SBL can be divided in three subclasses based on their turbulence characteristics (Van de Wiel *et al.*, 2003; Mahrt, 1999). Van de Wiel *et al.* (2003) suggested the following three regimes:

a) Continuously turbulent

b) Intermittent regime

c) Radiative regime

Examples of these SBL regimes are given in figure 1.3. Weakly stable SBLs (regime a) are likely to occur during cloudy and windy nights, where turbulence is continuously present. In contrast very stable boundary layers (VSBL) (regime b and c) occur during nights with calm winds and clear skies. Turbulence never completely vanishes in extremely stable conditions, but can be sporadically present in bursts of turbulence (intermittency). Turbulent intermittency occurs according to the following principle. When the turbulent exchange between surface and atmosphere is very small, the flow may decouples from the surface. The surface friction forces on the air diminishes and the air starts to accelerate. At some point, the wind shear exceeds a

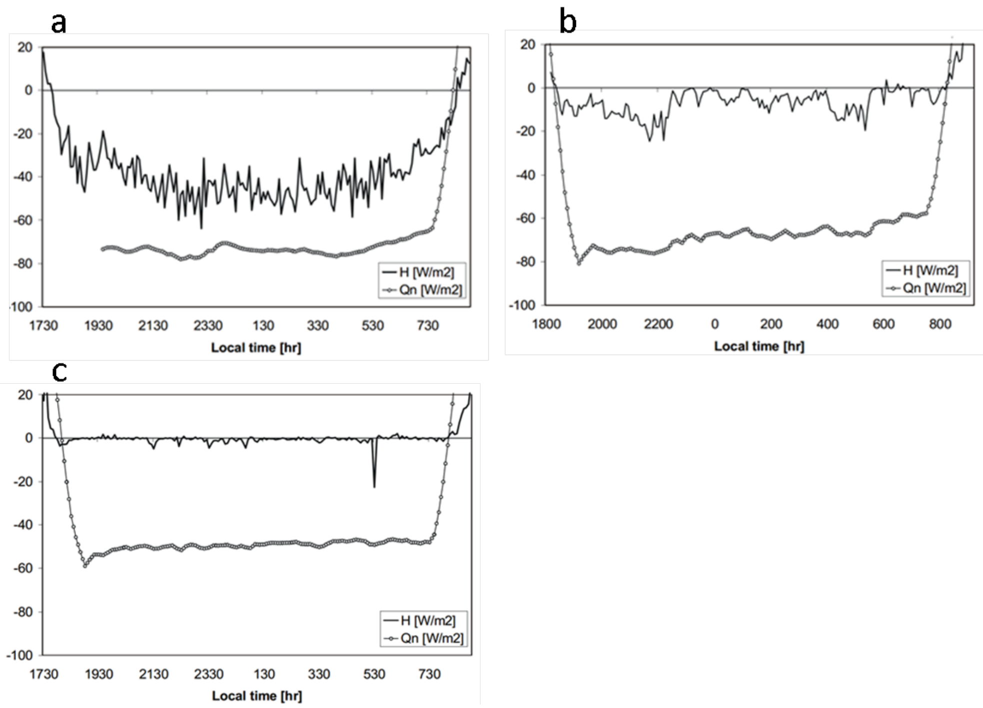

Figure 1.3: a) Weakly stable boundary layer with continuous turbulence. b) Very stable boundary layer with intermittent turbulence. c) Radiative regime with hardly any turbulence. From: van de Wiel (2003)

critical value and causes enhanced vertical mixing. The temperature gradient and wind shear are reduced and the stratification process starts over again.

In contrast to the weakly stable SBL, the theoretical framework of the very stable SBL is not well understood. Difficulties in studying the SBL are related to the scale dependence of turbulent fluxes. Hence similarity theory cannot easily be used to study weak turbulence, since the fluxes are small and mesoscale motions, like internal gravity waves and drainage flows, in turbulent flux measurements become important (Mahrt & Vickers, 2006; Sorbjan & Grachev, 2010; Howell & Sun, 1999). Recently, these non-turbulent motions with scales larger than the turbulent scale, but much smaller than the traditionally classified mesoscale processes are referred to submeso motions (Mahrt, 2009). Moreover, Baas *et al.* (2006) mentioned that flux-gradient relationships may be stronger due to self-correlation when analysing weak turbulence. As consequence of the complexity of VSBLs, numerical weather prediction models poorly perform under very stable conditions. Van de Wiel (2002) clearly showed that even simple non-linear SBL equations lead to large uncertainty and unexpected behaviour in predictions. At present, modelling the decay of turbulence (Nadeau *et al.*, 2011) and SBLs (Seaman *et al.*, 2012) are still challenging and more understanding is needed to improve weather forecasts under very stable conditions. Numerous studies encountered problems with modelling or scaling very stable conditions in the SBL and concluded that more physical understanding about submeso motions and weak turbulence should be gained from field experiments (Acevedo *et al.*, 2013; Mahrt *et al.*, 2013; Steeneveld *et al.*, 2009).

Typical features in the VSBL include internal gravity waves, forming of cold pools, drainage flows and microfronts. Drainge flows occur when cold dense air starts to accelerate downslope by gravity in very stable conditions creating a near surface jet (Stull, 1988). Figure 1.4 shows an example of the theoretical concept and characteristics of drainage flows from the paper of Monti *et al.* (2002). Typical for the drainage flows are the frontal head, rising motions in front, sinking motions behind, overturning waves, upside-down wind profile and strong stratification. Figure 1.4 shows the idealised representation with some these typical features. In reality, however, drainage flows interact with other submeso motions which makes them complex to study as a separated feature. As consequence, other definitions than drainage flows are often used and related to each other in literature. Sun *et al.* (2002) defines a density current (buoyancy/gravity currents) as fast moving cold air at the surface initiated by multiple processes including drainage flows. Mahrt (2010) relate microfronts to strong changes in wind and temperature, generated by mechanisms including gravity waves, leading edges of drainage flows, density currents and surface heterogeneity. Moreover, drainage flows are often referred to katabatic flows (across the valley) and channel flows (along the valley) in steep valleys, where density currents are more related to a relative flat terrain. Although the principle of drainage flows is the same, different variations are possible. Multiple definitions are used in literature to make a distinction, which can sometimes lead to confusion. The main difference between the different variations of drainage flows is the space/time scale. Drainage flows across deep valleys can for instance also exist in less stable conditions. In this thesis we will refer to the definition shallow drainage flows.

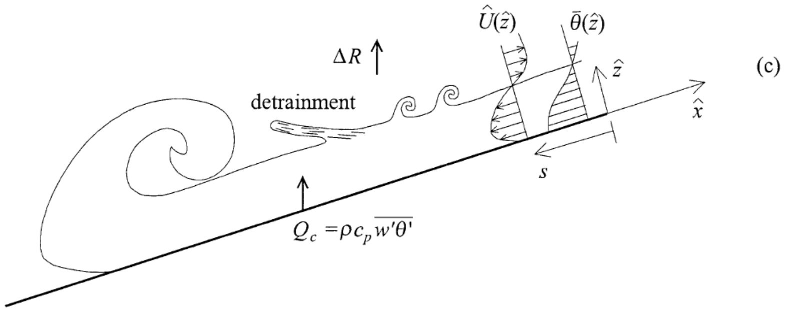

Figure 1.4: Theoretical concept of drainage flows from Monti *et al.* (2002). Including features are the frontal head, overturning waves, detrainment ,surface jet and strong stratification. The vertical extent changes from site to site.

In contrast to drainage flows over mountain slopes as studied by for instance Nadeau *et al.* (2012), drainage flows over gentle slopes has received little attention in literature. Soler *et al.* (2002) and Mahrt *et al.* (2001) analysed a thin drainage flow of only a few metres depth during the CASES99 campaign. Moreover, Brazel *et al.* (2005) identified slope flows in order of tens of meters in complex topography in the Phoenix area. Given the gentle slope and the extensive dataset of the BLASST campaign, the complex near surface motions can be studied in more detail.

1.2 Research Questions and Objectives

The aim of this thesis is to evaluate the fenology of near surface features in the VSBL by doing case studies. The main question of this study is: how does the BLLAST observations support and contribute to the current understanding of the physical background of near surface features in the VSBL? The focus will be on the radiative SBL regime as introduced in the previous section. The BLLAST dataset contains a limited amount of 11 IOP days which can be used for case studies. In the BLLAST dataset, we will search for specific near surface features and shallow drainage flow in particular. The two most suitable cases from the IOP days will be selected for further data analysis. The research questions are:

- Can drainage flow within 10m from the surface be identified during BLLAST?
- Which submeso motions are acting in the VSBL during BLLAST?
- What is the structure of the near surface vertical profile of the VSBL?
- What are the relevant turbulent scales?

After detecting shallow drainage flows in the BLLAST dataset, the following research questions are studied:

- How does the shallow drainage flow evolves?
- What are the driven processes of shallow drainage flows?
- How are the shallow drainage flows related to the field topography of the BLLAST area?
- How is turbulence described in shallow drainage flows?

The research framework as described in the Methods section will be used as guideline for this study. One of the objectives is to add new features to the theoretical concept of shallow drainage flow presented in figure 1.4 of the study from Monti *et al.* (2002). Another objective is to develop and review research techniques to study submeso motions in the VSBL.

The following chapter Material and Methods describes the measurement campaign, used data, data processing and methods used in this study. In chapter Results and Discussions, we start analysing the full dataset and then continue studying small segments of data. Finally, this chapter ends with a small syntheses of the analysed cases. Conclusions and recommendations can be found in the last chapter.

Chapter 2

Materials and Methods

2.1 BLLAST experiment

The BLLAST campaign was hosted by the instrumented site of Centre de Recherches Atmospheriques in Lannemezan, France and executed from 14 June to 8 July 2011 by various international groups. The experimental research site is from the Laboratoire d'Aerologie, which is in turn part of the Observatoire Midi-Pyrénées (University of Toulouse). The measurement area is close to the city centre and 30km North of the Pyrénées Mountains. The Pyrénées mountain range is east-west orientated and with summits around 2-3 km high. The experiments are conducted at two sites called Supersite 1 and Supersite 2 (figure 1.1 in Introduction), where we only use data from Supersite 1. During the campaign an extensive dataset is collected by multiple instruments including air planes, unmanned aerial vehicles, remote sensing instruments, sonic anemometers and radiosoundings. The campaign was designed to study the transition between the convective boundary layer and the nocturnal boundary layer. In contrast to the campaigns' objective, we use the data only to study the SBL.

2.1.1 Measurement Site

The Divergence Site at Supersite 1 (43° 07' 39.3" N ; 0° 21' 57.9" E) is covered with 10-20cm tall fresh grass on a hard-packed soil. Figure 2.1 shows a satellite picture and elevation map of the Divergence Site including the locations of the instrumentation. We use Eddy Covariance data from the Skinflow and Valimev tower, and Thermal Infra-red data from the field of the Skinflow EC. The elevation map shows a gentle SE to NW slope of approximately 7% (1.5°), hence drainage flows are expected from the SE. During very stable conditions cold air pools are expected to form in the surface depressions. A band of trees is located at geographically high point in the landscape, which may be of substantial importance on local flows as it increases the surface roughness. Moreover a small drainage gully (dark green line on the satellite picture) is present at the measurement site, but does not contain water.

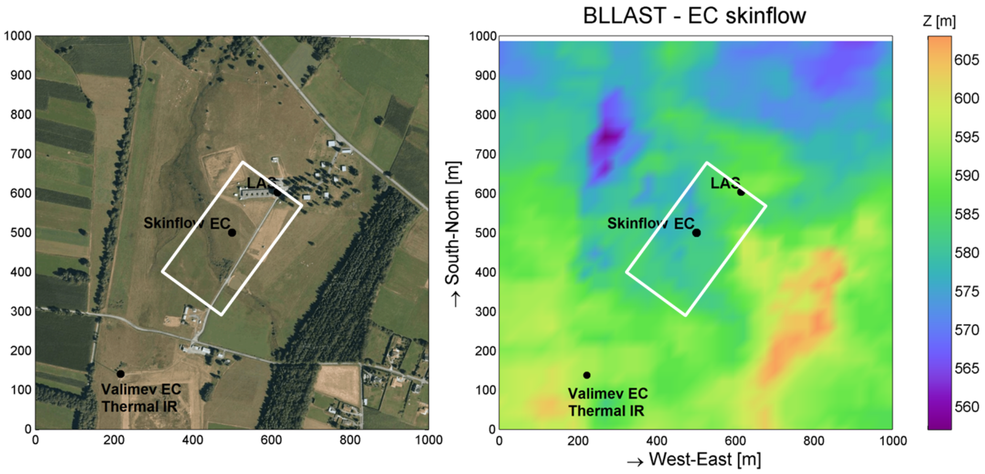

Figure 2.1: Left: Google Earth picture of Supersite 1. Right: Digital elevation map of the measurement field. The white box represents the area covered by the thermal IR camera.

2.1.2 Instrumentation

As mentioned before, we use three main datasets; EC data from the Skinflow and Valimev tower, and thermal infra-red (IR) data of the field. The next paragraphs give a extensive description of the different instrumentation. Table 2.1 shows an overview of the used instrumentation with their properties. Pictures of the experimental set-up of the used data is showed in figure 2.2.

The Skinflow EC tower has a height of 10 meters and is equipped with 2 Kaijo Denki sonic anemometers (KD) and 4 CSAT3 sonic anemometers from Campbell Scientific Inc.. The main difference between the KD and CSAT3 is the path length of respectively 0.05m and 0.1155m. Hence, KD sonics are better capable to measure smaller eddies, which are more dominant at the surface. All sonics measure the sonic temperature which is comparable to the virtual temperature. In addition, the EC sonics are installed with fast responding Campbell Scientific E-TYPE model FW05 thermocouples to measure air temperature. Unfortunately, the 1m low thermocouple did not work during the whole experiment. Additionally, 4 thermocouple wires of the same type are installed near the surface. All data are stored by a Campbell CR5000 data-logger. The Skinflow Tower was operational between 19 June and 9 July 2011. It must be noted that the 1m low KD sonic was not operational till 23 June.

The 60 m heigh Valimev tower is stationed approximately 350 m SW of the Skinflow tower. The tower is equipped with multiple instruments, where we only use three EC sonics at 30, 45 and 60 meter, water vapour data at 30 and 60 meter and thermal IR camera (table 2.1). The EC-stations were operational between 14 June and 9 July 2011. The thermal IR camera is looking downward to the Skinflow tower area till 29th of June. Hereafter, the camera view has changed to the Micro Site which is outside our measurement area. The IR camera measures the long-wave radiation in the mid-wavelength infrared spectrum (3-8 µm) from the field, which is an function of surface temperature and emissivity. The instrument makes images with a birds eye view with a spatial resolution of 1.36 mrad. After the coordinate transformation and interpolation, the rectangular grid resolution is dx=0.65m and dy=4.55m. Properties of the IR camera are the height z=59.02m above ground level, angle α = 49.2°, view angle of 1.36 mrad (BLL, 2011).

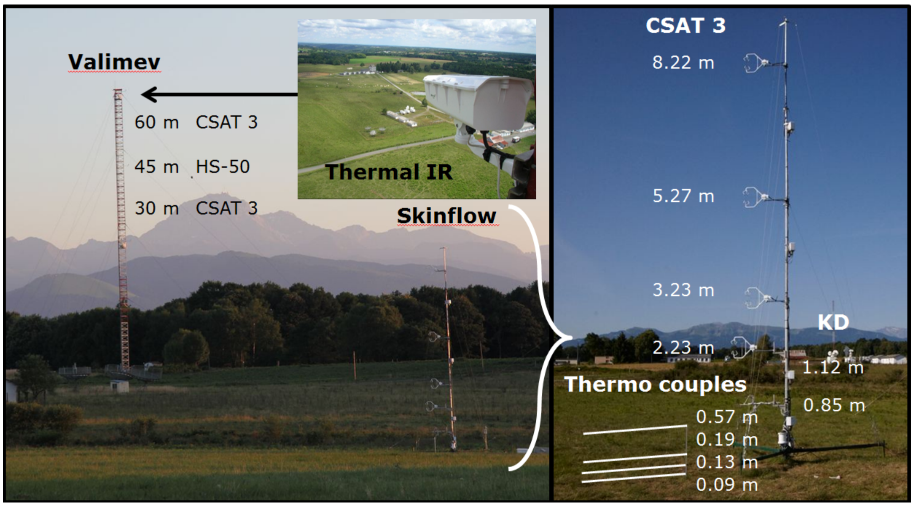

Figure 2.2: Pictures of the experimental set-up of the Skinflow tower at the Divergence Site and the Valimev Tower during the BLLAST campaign.

Table 2.1: Properties of the used intrumentation. Red: major equipment failure with affected parameters. Orange: Inconsistencies in data of less importance.

Parameters	Sensor Type	Height AGL [m]	In Thesis	Sampling Frequency
Skinflow Site				
u,v,w,T-son, T-air	KD-TR/90AH, Thermocouple (0.0127 mm)	0.85	1m low	20 Hz
u,v,w,T-son, T-air	KD-TR/90AH, Thermocouple (0.0127 mm)	1.12	1m up	20 Hz
u,v,w,T-son, T-air	CSAT3, Thermocouple (0.0127 mm)	2.23	2m	20 Hz
u,v,w,T-son, T-air	CSAT3, Thermocouple (0.0127 mm)	3.23	3m	20 Hz
u,v,w,T-son, T-air	CSAT3, Thermocouple (0.0127 mm)	5.27	5m	20 Hz
u,v,w,T-son, T-air	CSAT3, Thermocouple (0.0127 mm)	8.22	8m	20 Hz
T-air	Thermocouple (0.0127 mm)	0.091	0.09m	20 Hz
T-air	Thermocouple (0.0127 mm)	0.131	0.13m	20 Hz
T-air	Thermocouple (0.0127 mm)	0.191	0.19m	20 Hz
T-air	Thermocouple (0.0127 mm)	0.569	0.57m	20 Hz
Valimev Tower				
u,v,w,T-son, q	CSAT3, Licor 7500A CO2/H20 Analyser	29.3	30m	10 Hz
u,v,w,T-son	HS-50	45.8	45m	10 Hz
u,v,w,T-son, q	CSAT3, KH20 hygrometer	61.4	60m	10 Hz
T-surface	FLIR A320 IR camera	59.02		1 Hz

2.2 Data Treatment

The turbulence data used in this thesis are processed by the BLLAST campaign members and is available in raw data and 5,10 and 30 min averaged flux files (De Coster & Pietersen, 2011). However, raw data of the Valimev Tower were not available during this study. In addition, some of the data is alternatively processed during this study. Most important data processing and principles are described in the next sections. The most important data originates from the Skinflow Tower, while the Valimev Tower and thermal IR data will be used as additional datasets.

2.2.1 Turbulence Data

Raw Data

Raw data from the Skinflow Tower is stored in daily NetCDF files available for each EC station. During the processing, bad data is replaced by a dummy value. However, unrealistic values were still present in the raw thermocouple data. To eliminate the dummy values and unrealistic values from this dataset, a filter of 0-35°C is used. Some realistic temperatures >30°C during daytime might be deleted, but they are not of importance in this research. The sonic temperature of the KD 1m up station shows a negative offset of <1 °C and is removed when the KD 1m low level was available.

The lowest KD sonic from the Skinflow Tower already showed some troubles during the campaign. The signal of the w component showed obvious outliers and a transition to a large offset (figure 2.3). In order to use information of this sonic, the signal is cleaned by using an algorithm. The algorithm firstly removed outliers which deviate more than 1 m/s from the previous sample. In some cases, the outlier is captured in more than one sample, which are then removed afterwards. Now, the signal is cleaned from outliers. Secondly, the off setted signal is separated from the normal signal and the offset is calculated by a mean of the offset signal. Finally, the offset is corrected by subtracting the calculated offset from the separated signal.

Wind data from the NetCDF files are not yet rotated. Planar fit angles are calculated by

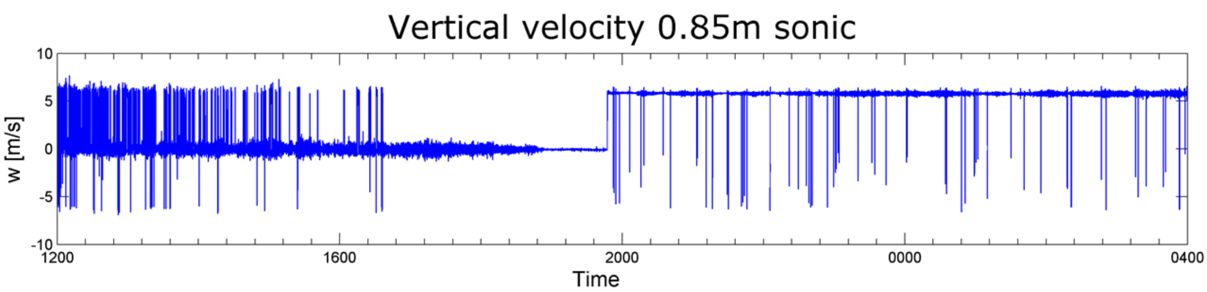

Figure 2.3: Example of the raw vertical velocity time record of the KD 1m low sonic. The signal contains both outliers and offset.

the program Planang according to the algorithm of Wilczak *et al.* (2001) in order to rotate the sonic in direction of the mean flow. The angles defines the plane of the mean wind for a specific time period. In addition, the bias of vertical velocity w is forced to be zero. As described above, however, a bad signal of the KD 1m low sonic is used to calculate the planar fit angles at this level. Hence, classic yaw and pitch rotations are performed for this EC-stations. All other stations are corrected with the planar fit method which performs pitch and roll rotations.

Averaged Quantities

The eddy-covariance software program EC-Pack is used to produce uniformly processed 5,10 and 30 min averaged flux files of both Skinflow and Valimev tower for each EC-level individually. The daily NetCDF files and planar fit angles are used as input to produce the means, variances, co-variances, fluxes and structure parameters, which are all stored in the flux files. A more detailed description of eddy-covariance data processing in EC-Pack is given in van Dijk *et al.* (2004). The thermocouples at the EC-levels were not always operational during the measurement period. In EC-pack, sonic temperature was used to extrapolate the thermocouple temperature data sequence. The next paragraphs describe the additional data processing actions, done during this study.

As consequence of the bad signal of the KD 1m low sonic, some variables like wind direction, heat flux, friction velocity and all other derived variables which make use of the vertical velocity signal cannot be used from EC-Pack. Friction velocity (u^*) and heat flux (H) are not easy to reconstruct from raw data due to multiple corrections in EC-Pack and are not replaced. The wind direction, however, is recalculated by using the corrected raw wind data as described above.

The four additional thermocouple levels next to the Skinflow Tower are not processed in EC-Pack. In order to have an uniform averaging method for the thermocouple data, the averaged thermocouple data will not be used from EC-Pack output files. Instead, both thermocouple temperature means and variances are calculated from the cleaned daily NetCDF data. Thermocouple data was not available in the Valimev Tower. The actual air temperature is then estimated by the following formula.

$$T_{cor} = \frac{T_{son}}{1 + 0.61q} \tag{2.1}$$

where T_{cor} $[Kelvin]$, T_{son} $[Kelvin]$ and q $[kg/kg]$ are respectively the corrected temperature, sonic temperature and the specific humidity. Note that we use specific humidity in stead of mixing ratio, which is valid under not excessively moist circumstances. We assume thermocouple and sonic temperature variances to be identical.

Besides the inconsistencies in uniformity of processed data, there were some issues concerning instrument failure. Sonic temperature values from the HS-50 instrument at 45m level seems to have a substantial offset compared with the CSAT-3 and are ignored. The offset has no consequences for the temperature variance,so σ_T^2 and H_{sonic} are conserved in the analysis.

2.2.2 IR Camera

Surface temperature values are calculated from the detected long-wave radiation. Detected long-wave radiation from the surface is partly absorbed and scattered by atmospheric gases, which causing a reduction in the measured radiation(II). Reflection by the surface from surroundings contributes to the detected radiation(III). Hence, formula 2.2 has been used to separate these processes and calculate the actual surface temperature(I),

$$V_{detector} = Tr\Big(\underbrace{\epsilon\sigma T^4_{object}}_{\mathrm{I}} + \underbrace{(1-\epsilon)\sigma T^4_{amb}\Big)}_{\mathrm{II}} + \underbrace{(1-Tr)\sigma T^4_{amb}}_{\mathrm{III}} \tag{2.2}$$

where Tr, ϵ, σ, T_{object}, T_{amb} and $V_{detector}$ are respectively the transmittance, emissivity, Stefan-Boltzman constant, object (surface) temperature, ambient temperature and total radiance. Used values for Tr and ϵ are respectively, 1 and 0.95.

The surface temperature data is stored in MATLAB data files which contains 320x100 values. To represent the surface temperature of the divergence site, a filter is used to set all pixels which does not represent grass to NoData.

2.3 Research Methods

This section describes the used research methods and their relevance during this study. The research approach is visualized in figure 2.4. The analysis tools are represented in single blocks and used for the case studies. The starting point is to select two nights which match extreme stability criteria. Secondly, research tools as showed in figure 2.4 are used to describe the evolution of drainage flows. In addition, the results will be used to construct a schematic representation of the drainage flows during BLLAST.

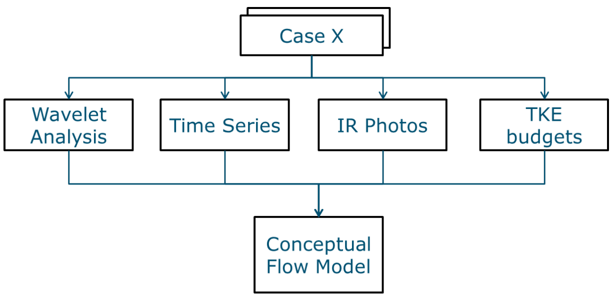

Figure 2.4: Schematic visualisation of the research strategy.

We search for extreme stable conditions in the BLLAST dataset in order to select cases. The z/L value is one parameter to quantify the stability. The Obuklov length $[L]$ is calculated by the following equation.

$$L = \frac{-\overline{\theta_v}\, u_*^3}{\kappa\, g\, (\overline{w'\,\theta_v'})_s} \tag{2.3}$$

where all variables are taken from 5 minute EC-pack output, $\kappa = 0.4$ and $g = 9.81$. The sonic temperature is used for θ_v and the buoyancy flux, since it approximates the virtual temperature. The sign of z/L is determined by the sign of the surface buoyancy flux which is normally negative during night. Hence, stable stratification is characterized by positive values of z/L, whereas high values represent high stable stratification.

Other indications for radiative boundary layers are sensible heat flux close to zero and low friction velocity. The cases are selected using the following criteria:

- IOP day
- H <-25 W/m2
- u^* <0.1 m/s
- z/L >1

The following sections will describe how time series, wavelets and TKE budgets are used to study near surface features in the VSBL.

2.3.1 Time Series

Since the focus is on very stable cases during BLLAST, small scale turbulence will be important. Therefore 5 minute averaged flux files will be used to detect near surface features. Time series of the near surface features will be studied at the sampling frequency of the instrument in order to study the events at the finest scales. Special attention will be on shallow drainage flows as already mentioned.

The time and vertical resolution of the data is very unique and a description of shallow drainage flow with such a high resolution of data has never been reported. Multilevel time series with high sampling frequency will give very detailed information of different atmospheric quantities. In this manner, we will be able to gain more understanding about the complexity of submeso flows. For the empirical description of shallow drainage flow, multivariate time series are used. Multivariate time series analysis is a common used technique in geo-sciences, which can be used for an empirical description of processes and the interaction between multiple parameters. Viana *et al.* (2010) widely used time series to study gravity waves on top of a drainage flow and showed that it is a sufficient method. However the use of multivariate time series is limited to explain physical laws, since atmospheric quantities are often non-stationary.

Important parameters to study shallow drainage flow are especially the wind profile and wind direction. In this thesis, we define shallow drainage flows as a condition with a wind maximum within 8m from the surface and a flow direction towards a geographically low area. Note that no data is available between 8m and 30m, hence deeper drainage flows cannot be detected. Once such an event is detected, focus will be on parameters such as vertical velocity (w), heat flux (H), temperature (T) and turbulent kinetic energy (TKE). The following equations are used to calculate the H [Wm^{-2}] and TKE [m^2s^{-2}].

$$H = \rho C_p \overline{w'T'} \tag{2.4}$$

where ρ, C_p, and $\overline{w'T'}$ are respectively the air density, specific heat and kinematic eddy heat flux. Fixed values for ρ ($1.2\ kg \cdot m^{-3}$) and C_p ($1004\ m^2 \cdot s^{-2} \cdot K^{-1}$) are used, because no humidity data was available.

$$TKE = \frac{1}{2}(\overline{u'^2} + \overline{v'^2} + \overline{w'^2}) \tag{2.5}$$

2.3.2 Wavelets

Wavelet analysis is one of the techniques to study atmospheric turbulence. The benefit of wavelet analysis is that time series can be studied in a time-frequency domain rather than only a time domain. Hence, fine features can be separated from large scale features and their contribution to the total variance can be quantified. Moreover, wavelet analysis is a better tool to study non-stationary time series compared to Fourier Analysis. (Kumar & Foufoula-Georgiou, 1997).

Another common used tool to study atmospheric turbulence are ogive curves as introduced in Oncley *et al.* (1996). The area under the spectral density plot represents the total variance captured in the time record. Ogives are constructed from turbulence spectra by integration of the power spectral density over the time scale domain. The integration starts at the smallest time scale, where the cumulative variance is zero. Two schematic representations of a ogive are showed in figure 2.6. The ogive curve is very suitable to study the distribution of total variance over the frequency domain. The ogive curve quickly shows the corresponding time scale where almost all variance is reached and thus useful to determine the averaging time of turbulent fluxes.

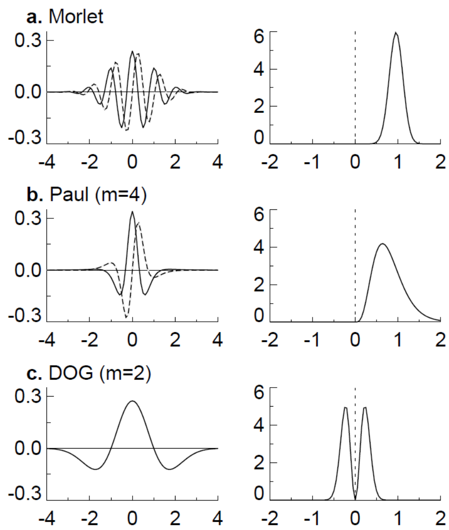

Figure 2.5: Three different wavelet bases, where the left pictures shows the real (solid) and imaginary (dashed) of the wavelet in the time domain. Right pictures shows the wavelet in the frequency domain. From Torrence & Compo (1998).

In this thesis, the wavelet toolbox of Compo and Torrence is used for the wavelet analysis (Torrence & Compo, 1998). The toolbox calculates a wavelet transform and contains three different wavelet base functions; Morlet, Paul and Dog. Variations in wavelet base functions and parameter number (wavenumber or order) will influence the results, as well as the sampling interval of the time series. Using a Paul wavelet or smaller parameter values provides better accuracy in the time domain, while a Morlet wavelet or larger parameter values increases the accuracy in frequency domain (De Moortel *et al.*, 2004). The DOG wavelet is less suitable to use for oscillatory behaviour, because it is real valued in contrast with the Morlet and Paul wavelet which also has a complex part. There is not a predefined wavelet or parameter value which provides the best results with respect to stable boundary research. Multiple options variations are tested in order to receive the best results.

Ordinary wavelet analysis can be used to identify special events with a specific time scale. However, it is sometimes hard to make a good representation of the event in a wavelet graph. Moreover, some time periods are not related to a certain time scale and the spectral information is then lost in the graph. In order to receive all information of involved time scales during an entire night, we developed a new method to represent this information. The new method, here named as ogive-wavlet, combines the benefits of both ogives and wavelets (Hartogensis, Pers. com, 2013).

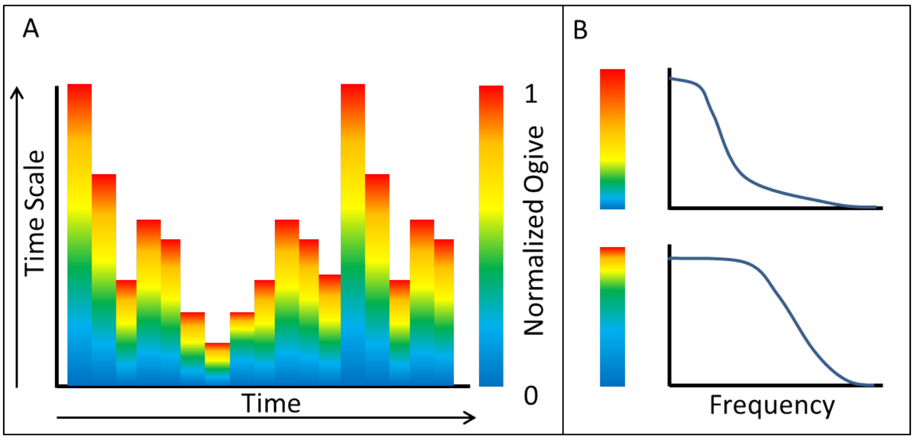

Figure 2.6: A: Schematic representation of the wavelet-ogive method. In practice, the bars will be small lines due to the large amount of data. B: Schematic representation of the relation between the ogive curves and colors. Variance dominated by relative small time scales in the spectrum refer to more bluish colors. Reddish colors visa versa.

The ordinary wavelet method involves time scales between half the sampling frequency and the record length. The scales in the SBL vary continuously between turbulent scales and mesoscales and are not well-defined, which forms one of the challenges in SBL research with respect to statistical theories (Mahrt *et al.*, 2009). When studying fine structures during an entire night, large structures can dominate the spectral analysis which makes it hard to analyse and identify fine structures during the entire night. In this thesis, we want to concentrate only on fine scale structures. Therefore, a wavelet filter is build in to filter out wave-scales larger than the wave filter. Scales much shorter than the record length can be studied more easily, while we can still study an entire night in a single time without involving very large time scales in the analysis. A schematic representation of the ogive-wavelet is shown in figure 2.6A. The colorbar is related to shape of the ogive curve as figure 2.6B shows. One ogive represents one line in the graph. In other words, a value (color) is assigned to a time scale which corresponds to a certain percentage of cumulated variance. The main benefit of this representation is that the involved time scales become directly visible from the graph. Hence, periods with high or low intensity of turbulence can be distinguished. Moreover, this tool can helps to determine averaging time scales for fluxes.

2.3.3 Turbulent Kinetic Energy

Budgets of TKE are made in order to study the significance of various processes causing turbulence generation or destruction. The TKE budget equation is shown in equation 2.6. The left hand side is made up of the local storage of TKE (Term I) and the advection of TKE (Term II). The TKE production and loss processes are given at the right hand sight, where term III represents the buoyant production/loss, term IV the mechanical shear production/loss, term V the turbulent transport of TKE, term VI the pressure correlation term and term VII the viscous dissipation of TKE. Buoyancy is a loss term during statically stable conditions over land, when the buoyancy force is negative. Mechanical shear is then expected to be the main source of TKE.

$$\underset{\text{I}}{\frac{\partial \overline{e}}{\partial t}} + \underset{\text{II}}{\overline{U}_j \frac{\partial \overline{e}}{\partial x_j}} = \underset{\text{III}}{+\delta_{i3}\frac{g}{\overline{\theta}_v}\left(\overline{u_i'\theta_v'}\right)} \underset{\text{IV}}{- \overline{u_i'u_j'}\frac{\partial \overline{U}_i}{\partial x_j}} \underset{\text{V}}{- \frac{\partial\left(\overline{u_j'e}\right)}{\partial x_j}} \underset{\text{VI}}{- \frac{1}{\overline{\rho}}\frac{\partial\left(\overline{u_i'p'}\right)}{\partial x_i}} \underset{\text{VII}}{- \varepsilon} \tag{2.6}$$

$$\underset{\text{I}}{\frac{\partial \overline{e}}{\partial t}} = \underset{\text{III}}{+\frac{g}{\overline{\theta}_v}\left(\overline{w'\theta_v'}\right)} \underset{\text{IV}}{- \overline{u'w'}\frac{\partial \overline{U}}{\partial z}} \underset{\text{V}}{- \frac{\partial\left(\overline{w'e}\right)}{\partial z}} \underset{\text{VI}}{- \frac{1}{\overline{\rho}}\frac{\partial\left(\overline{w'p'}\right)}{\partial z}} \underset{\text{VII}}{- \varepsilon} \tag{2.7}$$

If we align our data with the mean flow, neglect subsidence and assume horizontal homogeneity, equation 2.7 can be used for the analysis. Fluxes from EC-Pack will be used to calculate the budget terms, where the averaging time will be chosen based on the wavelet analysis. The dataset does not allow us to calculate term V and VI, so these will be captured in a rest term. Term I is calculated using equation 2.5 to calculate the turbulent kinetic energy e. Then, the derivative is approximated by using a piecewise cubic hermite interpolating polynomial to interpolate between data points. The polynomial is then used to estimate the derivative. Term III uses the sonic temperature T_{son} to approximate θ_v and g=9.81. The wind speed gradient in term IV is obtained likewise the derivation of the tendency term I using the horizontal wind. The TKE dissipation rate, term VII, can be estimated from the spectra by calculating an average dissipation rate by using the -5/3 scaling law of the TKE spectrum inertial-range as represented by equation 2.8 (Hartogensis *et al.*, 2002).

$$S_u = \alpha\epsilon^{2/3}\kappa^{-5/3} \tag{2.8}$$

Herein, S_u is the spectral density of the horizontal wind, α is the Kolmogorov constant and κ is the spatial wave number. The power-spectrum of horizontal wind is calculated by Fast Fourier Transformation in Matlab. Average wind speed is also used as parameter to calculate the dissipation.

Chapter 3

Results and Discussions

3.1 Cases Selection

As described in the Introduction, features in the VSBL will be studied during the BLLAST campaign by doing case studies. Hence, suitable cases should be selected at first. Calm weather conditions with clear skies are preferred to study the VSBL and are related to surrounding high pressure systems. Either anticyclonic or post-frontal dominated weather conditions are suitable for our case studies. A distinction between these conditions can be made from the mesoscale flow. Anticyclonic conditions correspond with a North-Easterly mountain-plain circulation compared to a North-Westerly dominated flow during post-frontal conditions.

The sensible heat flux $[H]$, friction velocity $[u^{*}]$ and z/L are used to quantify the stability. The sensible heat flux and friction velocity are taken from the 5 minute output of EC-pack. In addition, z/L is calculated according to the Obuklov length scale in equation 2.3. A time record of these stability parameters are presented in figure 3.1. Axes are adjusted to SBL specific values to see more detail in case of stability. The IOP (Intensive Observation Period) days are indicated by black arrows. During the IOP days, additional observations (like air vehicles, frequent radiosoundings) are done other than the continuous observations.

Small negative fluxes, low friction velocity and high z/L indicate stable conditions. Figure 3.1 shows several night with low fluxes which do not exceed -25 W/m2 in general. Combined with low values of u_{*}, the following nights starting from the evening before are suitable for further investigation: 19-06, 20-06, 24-06, 02-07 and 04-07. Analysis of surface temperature cannot be done for dates later than 30-06, because the field of view of the camera was changed towards a different site. Taken this into account, 20-06 (IOP3) and 24-06 (IOP4) are selected for further analysis. Both dates showing large z/L values, thus indicating very stable conditions. Note that z/L is only applicable in the surface layer, so measurements at 2m requires a boundary layer of 20m. In very stable conditions this might not be the case.

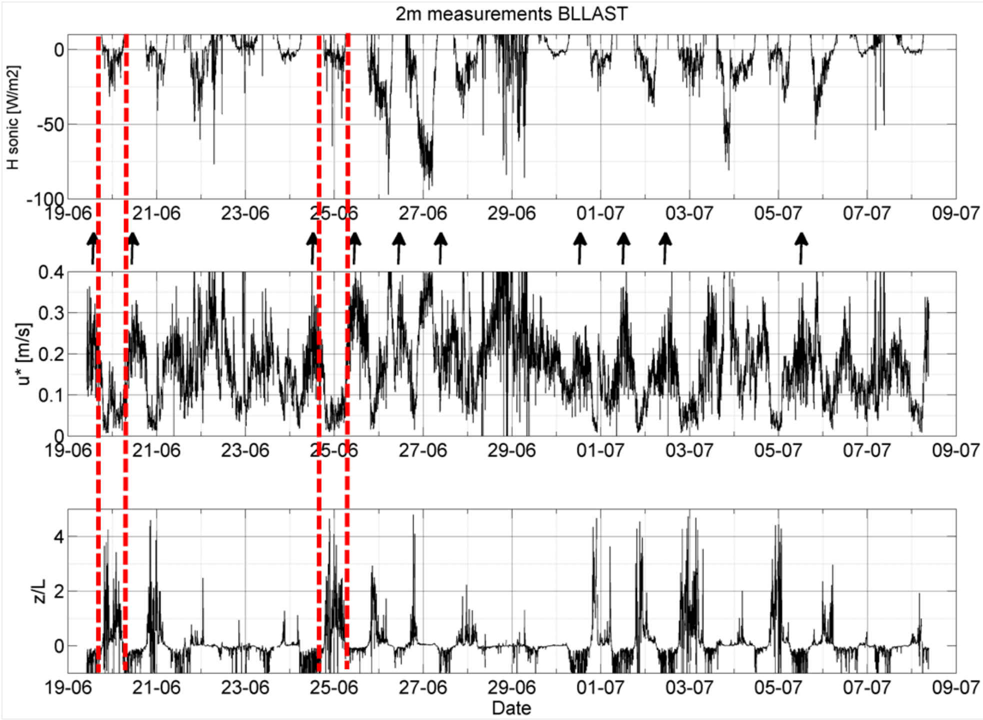

Figure 3.1: Calculated stability parameters of the BLLAST campaign. The black arrows indicate the IOP's during the experiment. The selected cases are indicated by the dotted windows.

3.2 Detailed Description

Large and Mesoscale Conditions

A daytime and nighttime wind distribution graph at 2m level of both 20-06 and 24-06 is visible in figure 3.2, where the colors represents discrete flow velocities intervals in m/s. Wind directions are plotted as wind vane.

The mountain-plain circulation becomes directly clear from figure 3.2. Low synoptic forcing during daytime causes a mountain-plane circulation with an anabatic wind blowing to the Pyrenees in the south. Moreover, it is clear that the daytime mesoscale conditions of both cases are not identical. A north-easterly wind at the surface dominates the flow pattern at 20 June, indicating anticyclonic conditions. The flow pattern at 24 June is more dominated by a north-westerly wind direction than a north-easterly flow, thus suggesting a transition between post-frontal and anticyclonic conditions. The nightime distribution graphs show a SSE flow pattern for both cases. However, the circulation changes during night of 20 June with light winds from the SSE, while strong winds are predominantly coming from the West.

The IOP summary report of Pino & Villa (2011) showed that the mountain-plane circulation on 20 June is around 250m deep during night and around 1km deep during day. The transition from downslope to upslope flow changes gradually in the vertical direction. In contrast to this case, a more abrupt transition in circulation takes place around z=750m on the evening of 24 June.

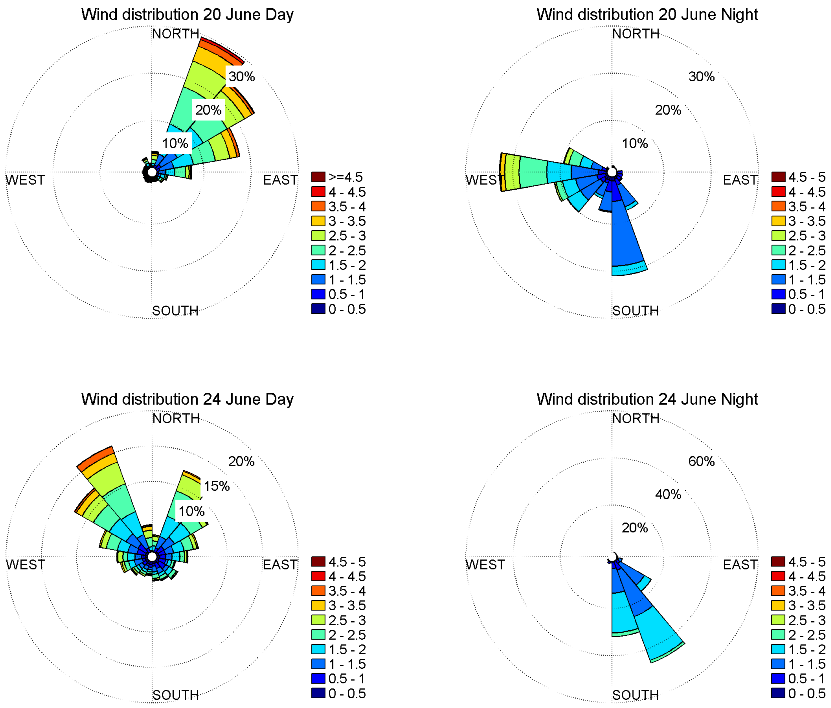

Figure 3.2: Left: Daytime distribution of wind speed and velocity at 2m level between 0900-1800 UTC. Right: Nigh time distribution at 2m level between 2000-0500 UTC. Wind direction corresponds with the wind vector direction (pointing in direction of the flow). The data is averaged over 10s intervals (3240 datapoints) in order to neglect irrelevant shifts in wind direction.

Evolution of Near Surface Vertical Profiles

Time series of vertical profiles for multiple quantities are made in order to have a quick overview of the SBL. We choose for quantities regarding the description of winds (u^*, σ_w^2, U) and heat (H_{sonic}, σ_T^2, T) in the boundary layer. The first case (20-06) and second case (24-06) are visible in figure 3.3 and 3.4 respectively. The first paragraphs will introduce the graphs, hereafter the interpretation follows.

The figures are build up from 5 minute averaged data as described in subsection fluxes and variances from section 2.2.1. The scatter function is used to place the quantity at a certain height and time. The height on the y-axis is represented on a log-scale, except for the wind vector graph. The color represents the value of a certain quantity. The range of the colorbars are adjusted in order to focus on very stable conditions. Hence, values outside the colorbar range does exist. The temperature and temperature variance profiles include 4 more levels originating from the additional thermocouple data. The vectors in the wind speed graph are pointing in direction of the flow (wind vector, not wind vane). The following sections will discuss the vertical structure chronologically, starting with 20 June.

20 June: Evening Transition Sun sets at 19:41 UTC at Lannemezan on the 20th of June, however negative sensible heat fluxes are already measured more than a hour before. Concerning accelerating wind speeds and shifting wind directions around midnight, thin high clouds related to an approaching front might block the solar radiation. The vertical velocity variance shows the decay of turbulence starting from the surface. Simultaneously, frictional velocity decreases, temperature variance increases and a stable layer is created. Wind speeds are decelerating during the evening transition to velocities <0.5 m/s. The mesoscale mountain-plane circulation changes to downhill flow (SSE) at the surface as earlier showed in figure 3.2.

20 June: Nocturnal Boundary Layer The nocturnal boundary layer can be split in two periods. The first period from 20:00-00:00 UTC is very stable with an heat flux around 0 W/m^2 and a strong stratification. Around midnight, a synoptic or mesoscale scale forcing causing mixing in the stable boundary layer and destroys the strong stratification. All quantities are not constant with hight except the sensible heat flux.

During the first part, the SBL is characterized by very small fluxes around zero, low u^* and low σ_w^2. Moreover, the temperature variance >30m is almost continuously very close to zero. The temperature at 30m is completely decoupled from the intermittent turbulence at the surface. These are indications of a very shallow SBL with weak turbulence. Two strong cooling events occurred at the surface which are closely related to very calm winds. A slight increase in wind speed causes near surface temperatures to increase with $\pm$ 2°C and so depicting the sensitivity of strong stratification in the SBL. The maximum stratification $\Delta T_{0.09-30m}$ of 7.4 °C was measured at 22:30 UTC.

Wind velocities within 10 meters are around 1.5 m/s and showing some variation in direction and magnitude. Wind is veering (turning clock-wise) with height and the vertical directional shear is initially low, but increases due to veering wind directions above 10m. The wind direction clearly shows the decoupling lowest layer from higher levels >10. Indications of an upside-down wind profile within 10m are found between 20:00-23:00 UTC with a maximum jet around 2-5m. Regarding the gentle slope of the measurement site, it is likely that drainage flows occur during this night. A more detailed description of this case is presented in section 3.3.

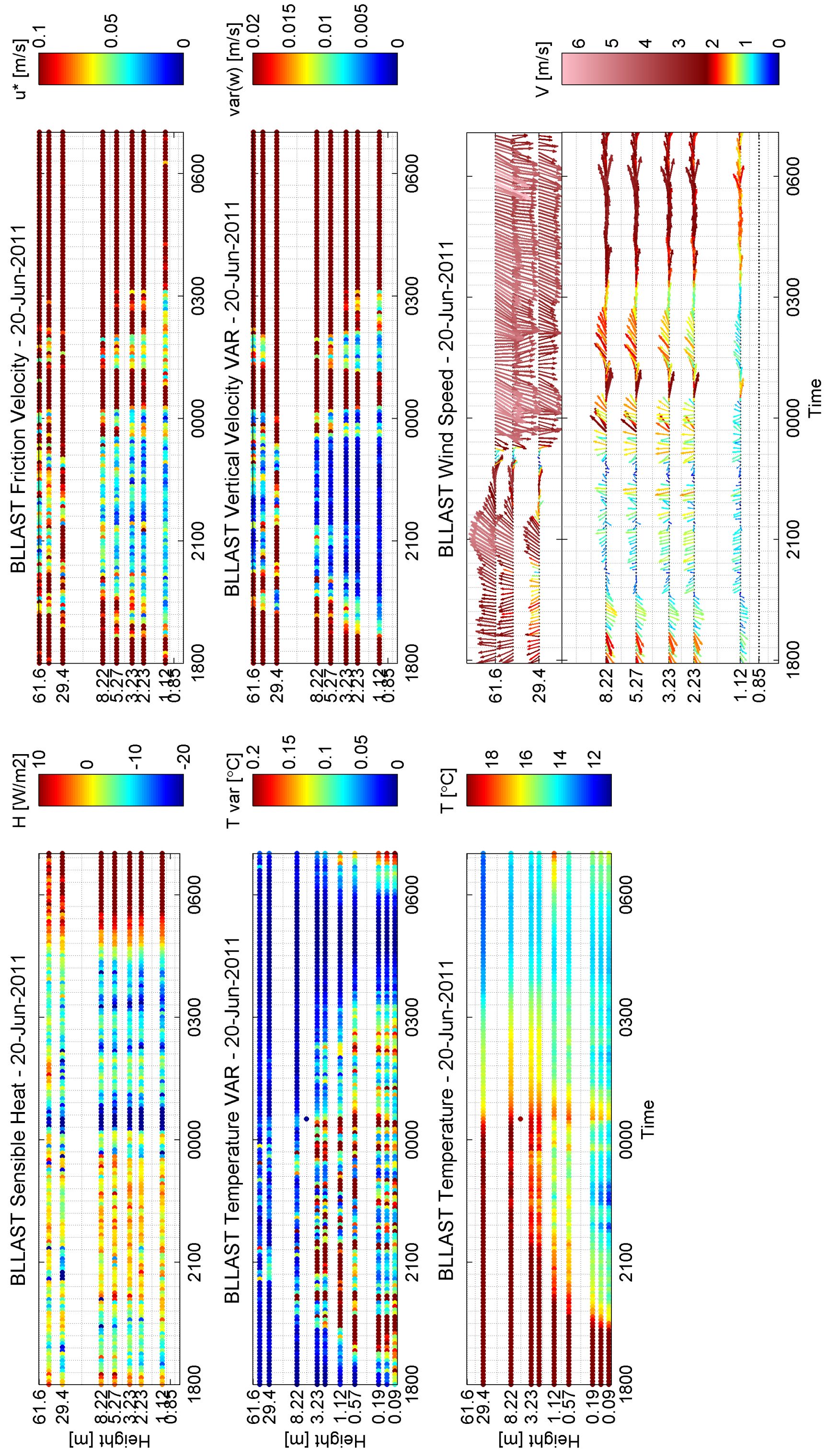

Figure 3.3: Vertical profiles of 5 minute averaged data from the evening of 20 June till the next morning. The single dots refer to single 5 minute averaged data points with a certain value. The 60m sonic temperature appeared to have bad data and is deleted. The wind vectors are pointing in the direction of the flow (wind vector).

24 June: Evening Transition An evening transition period can be distinguished around sunset at 19:37 UTC on the 24th of June. During the evening transition the heat flux changes from a positive to a negative sign (downward flux), hence a temperature inversion start to build up. Likewise, the mesoscale circulation changes from an uphill to a downhill flow (SSE wind direction) close at the surface. In between a period of almost zero flow velocities is visible. At higher elevations, the change in circulation is more gradually and lagged 2 hours compared to the surface. The collapse of turbulence is also visible in u^* and σ_w^2, which are both measures for turbulent activity. The graphs nicely show that the decay of turbulence starts at the surface, while higher altitudes are still turbulent.

24 June: Nocturnal Boundary Layer The heat flux in the nocturnal boundary layer is almost continuously very low, indicating extreme stable conditions. Hence, the nocturnal boundary layer can be classified as a radiative stable boundary layer in general. Although, a few moments of intermittency are represented in the graph, characterized by a higher deviation in vertical velocity and higher friction velocities. A short and intensive intermittency event takes place at 22:43 UTC which breaks even through the 60m level. Minimum heat fluxes up till -90 W/m^2 are measured, exceeding the colour scale of the graph. Apart from this event, the 60m level has a flux close to zero and it is likely that this level is already in the residual layer most of the time.

The temperature and temperature variance graph also support extreme stability with a shallow boundary layer. Most temperature variations occur close at the surface, whereas temperature variance is hardly present at 8m already. Moreover, the temperature decrease at levels >30m is only around 3°C during the entire night. The vertical temperature difference in the SBL varies a lot with a maximum $\Delta T_{0.09-30m}$ of 11.6 °C (22:15 UTC).

The intermittent behaviour of the stable boundary layer is clearly visible from the wind vector graph. Calm wind conditions are interrupted by higher wind speeds when the wind shear becomes too large, as result of decoupling, to hold the extreme stable situation. Friction velocity shows a very chaotic and complex patterns. Around 20:00 UTC, the wind profile starts to deviate from a normal situation with wind speeds decreasing with height. This suggests a decoupled boundary layer where winds are able to accelerate due to the disconnection of friction forces from the surface. The figure shows a wind maximum between 2 and 3 meters between 20:15-21:15 UTC with intensities around 2 m/s. An extensive analysis of the flow will be discussed in section 3.4 to understand the evolution and impact of the flow.

Compared to the 20 June case, the 10m layer is less decoupled from higher levels with respect to the wind direction. Moreover, the behaviour of the SBL appears more intermittent. However, the near surface jet is much stronger present in this case. Also note that the temperatures are around 5 °C colder compared to the previous case.

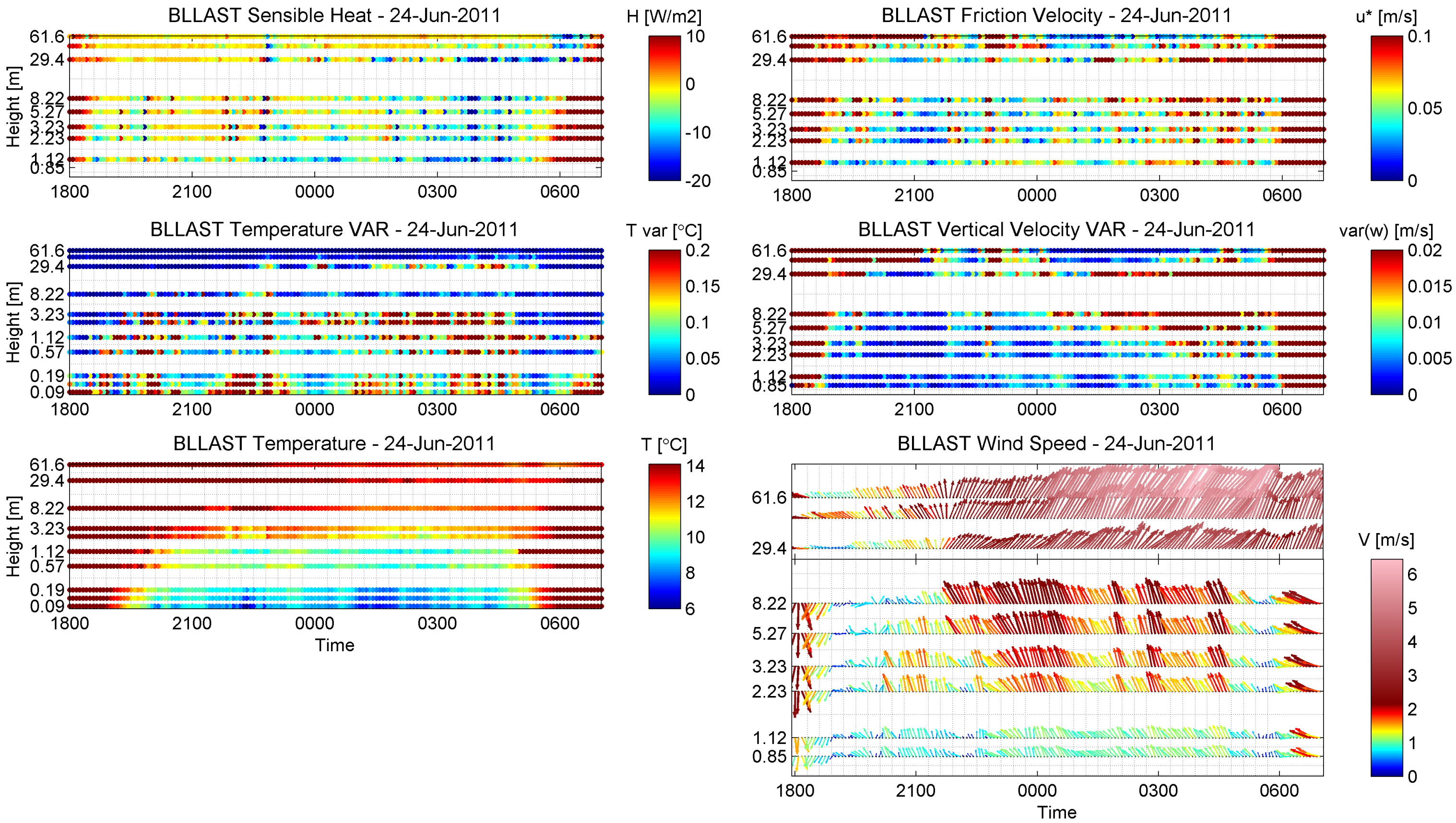

Figure 3.4: Vertical profiles of 5 minute averaged data from the evening of 24 June till the next morning. The single dots refer to single 5 minute averaged data points with a certain value. Sensible heat and friction velocity of the 0.85m level are deleted, because of impropriate processing of a wrong signal. The wind vectors are pointing in the direction of the flow (wind vector).

Time Scale Analysis

Investigating time scales is useful to determine the averaging time in order to calculate variances, covariances and fluxes. To show the involved time scales we use the new developed wavelet-ogive method as introduced in the previous chapter. This method uses a wave base function to calculate the spectrum. As already mentioned, the wave base function and parameter influence the results. Our main interest is the time scale of the VSBL features, so it is more useful to choose a wavelet with a high resolution in the frequency domain. Hence we choose for the Morlet (n=6) wavelet, because it shows more detail in the frequency domain compared to the Paul wavelet.

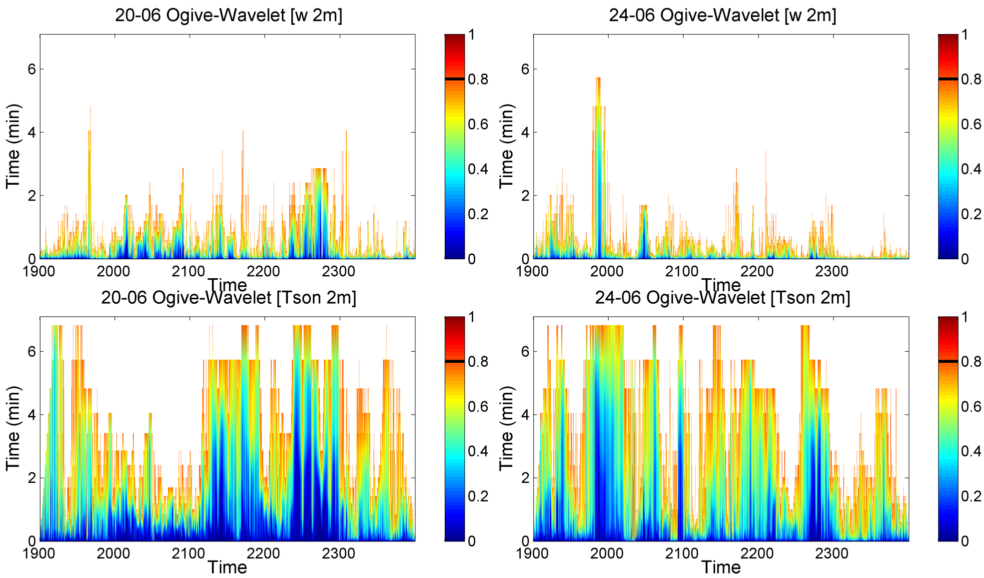

Figure 3.5: The Ogive-Wavelet results for the quantities vertical velocity (w) and sonic temperature (Tson) at 2m for both 20-06 and 24-06. The black horizontal line in the colorbar indicates the cut-off of the Ogive curve (0.8).

Results of the analysis for both cases are shown in figure 3.5. The results are achieved by delimiting time scales larger than 10 minutes. Moreover, the ogive is cut off at a point where 80 percent of the total variance is reached. The latter 80-100 percent of the variance is typically related to submeso processes in very stable conditions and is spread over a wide range of scales. Non turbulent processes in the submeso range (e.g. shallow drainage flow) should preferably be removed from the quantification of SBL similarity theory used for SBL modelling. However, this low frequency (non turbulent) processes might contribute to turbulence generation due to wind shear (Acevedo *et al.*, 2013). Here, we try to determine the averaging time scale for turbulent fluxes by excluding the submeso range.

Peaks in the graphs correspond to a time scale where 80 percent of the variance is reached. For both cases, the time scales of w are smaller than T_{son}. Most of the w variance is captured between 2-3 minutes, compared to 5-7 minutes time scale of T_{son}. The second case of 24-06 is more stable, considering w as measure for turbulent activity. Small bursts of turbulence, especially at 20-06, showing the intermittent behaviour of the SBL. Averaging time scales between 1-3 minutes are defensible based on the spectra of w. However, use of cospectra is more useful to determine averaging time scales for fluxes. An example of the w_{Tson} ogive-cowavelet is showed in figure 3.6. Unlike normal variances, negative values of covariances are possible. Negative contributions to the co-spectral variance appeared to be challenging to deal with and causing discontinuities in the graph. This issue negatively affects the readability of the graph. However valuable information can still be extracted by using this method. Use of 3 minute averaging time scale is also, most of the time, supported by the co-wavelet of wT.

Note that both too short and too long averaging time scales introduce errors in the flux estimations. Choosing a too short averaging time leads to a systematic underestimation of the (co)variance. Furthermore, shorter averaging intervals introduce a larger random error (more uncertainty) due to less independent samples (Van Kesteren, 2012).

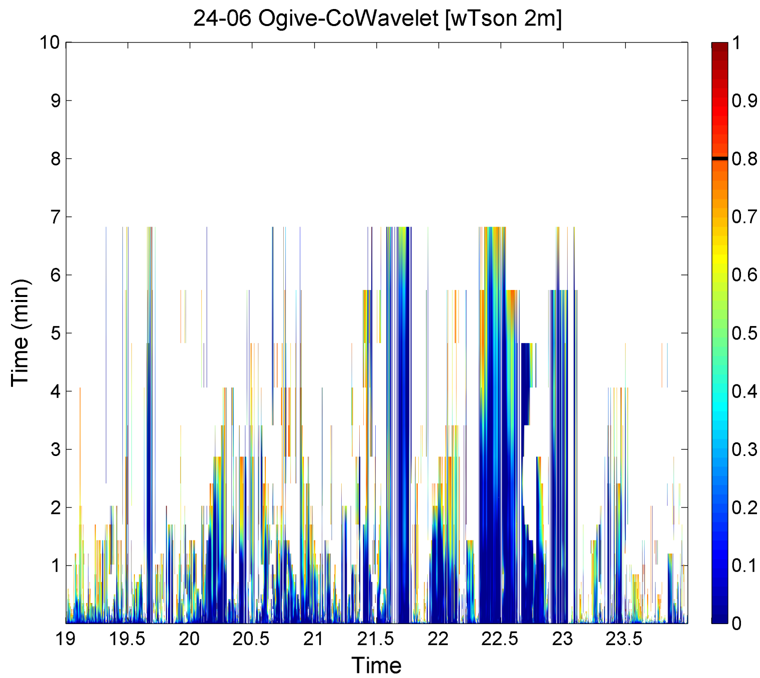

Figure 3.6: Example of a cowavelet-ogive from wT during 24-06.

3.3 Case 1: Drainage Flow 20-06

In the previous sections we depicted the extreme stability during two selected cases including a shallow drainage flow event. The following sections will concentrate on the first possible drainage flow event on the 20-06. Such a flow can only occur in very stable conditions when local surface heterogeneity becomes more important relative to the synoptic flow. We will try to relate the evolution of atmospheric quantities to the surface characteristics. The main objective is to understand flow and relate the evolution of atmospheric quantities to each other.

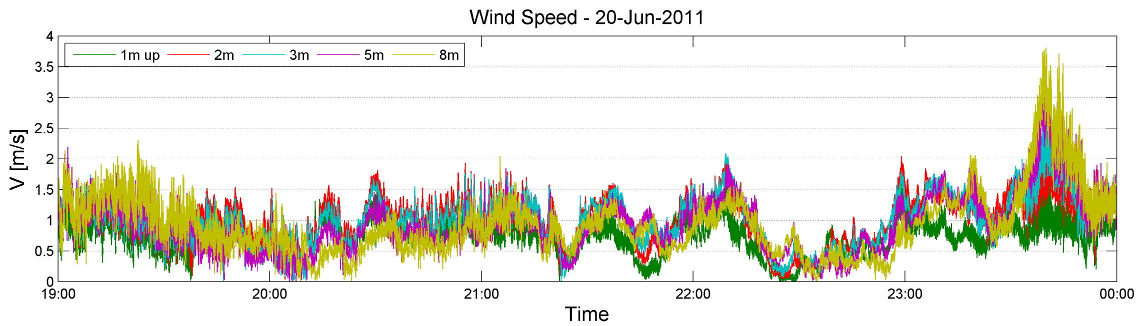

Figure 3.7: Time series of wind speed from 20Hz EC data at 5 levels during the early evening of 20-06. The series showing multiple oscillations and an upside-down wind profile.

Drainage flow main features

The time evolution of the wind profile in the previous section already shows an upside-down wind profile existing between approximately 20:00-23:30 UTC. Time series of horizontal wind speed are showed in figure 3.7 for 5 EC levels. The drainage current seems to behave in clear wave-like patterns although a more chaotic period is visible around 21:00 UTC. Duration of the wave cycles varies between 10 minutes to almost 1 hour, which are typical submeso scales. Note that this scale range is eliminated from the ogive-wavelet time scale analysis of w and T. However some small waves can be distinguished in between the major wave cycles. Clear detailed examples of this wave-like patterns in wind speed during drainage flow has not been found in literature.

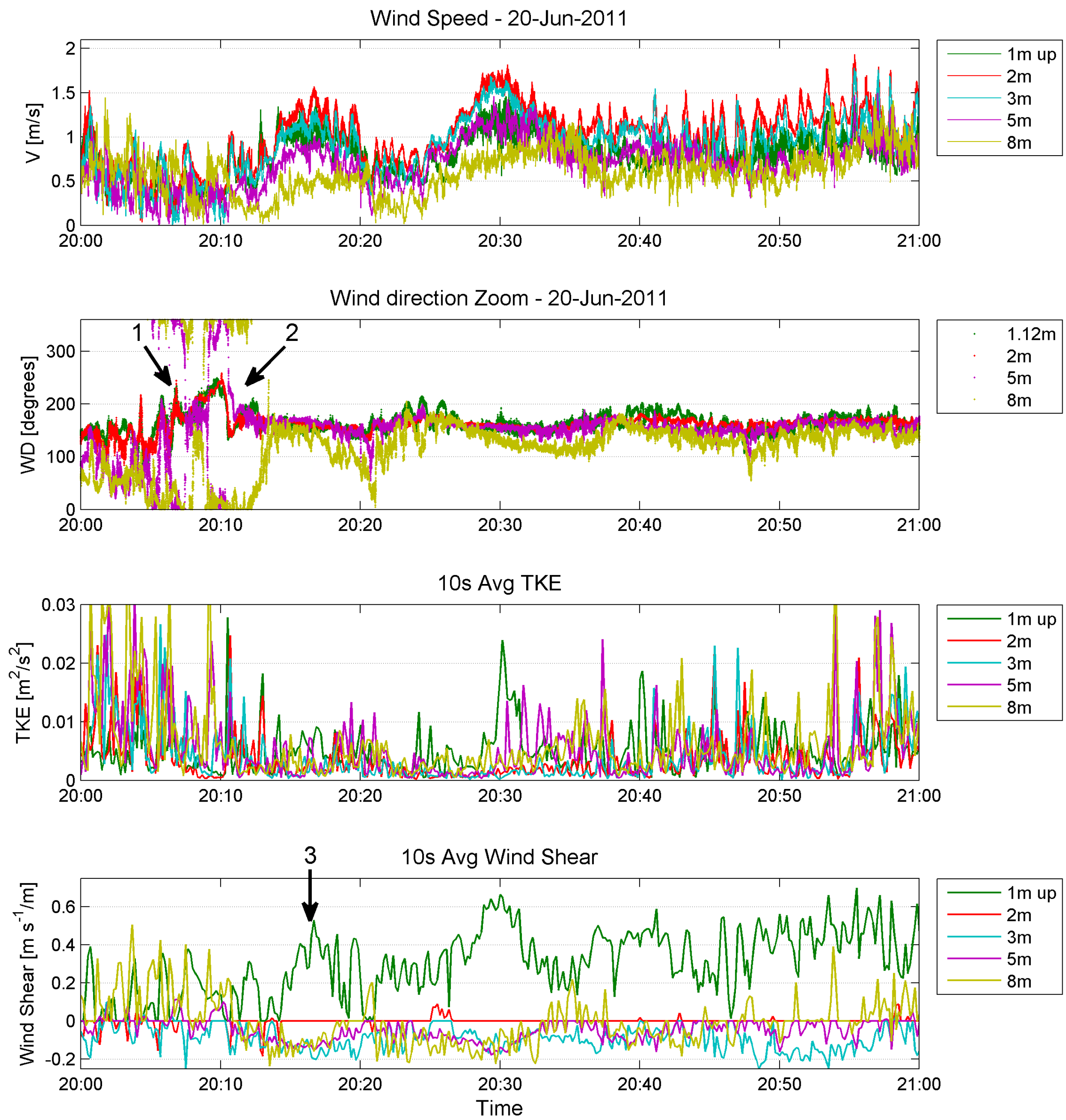

Figure 3.8: From up to down. 1) 20 Hz wind speed. 2) 20 Hz Wind direction. 3) TKE from 10 sec variances. 4) 10 sec averaged wind shear (wind gradient)

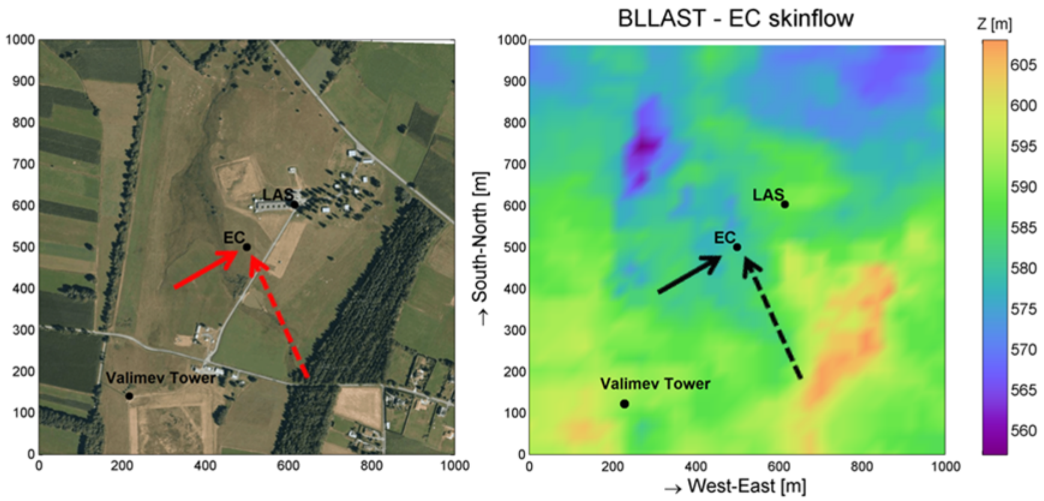

Figure 3.9: Typical flow directions represented in an aerial photo and the digital elevation map. The dotted arrow (155 degrees) represents the flow direction during the drainage flow. The solid arrow is related to warm air advection from the moist drainage gully.

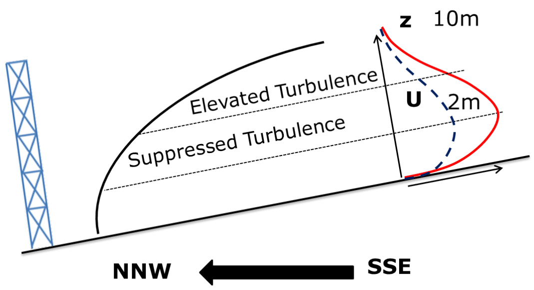

Figure 3.10: Schematic representation of the shallow drainage flow structure.

For the analysis we choose the period between 20:00-21:00 UTC, because it contains regular wave cycles pattern as well as a more chaotic part. We are willing to detect the origin of this difference. Note that the distinction between these two parts were already visible in the ogive-wavelet of temperature of figure 3.5. Time series of wind speed, wind direction, TKE and wind shear of the time period 20:00-21:00 UTC are represented in figure 3.8. The most convincing feature can be found in the sudden shifting wind direction of ±100 degrees just before the drainage flow arrives at the measurement station at 20:10 UTC, indicated by arrow 1 and 2. The wind gradient in figure 3.8 shows negative values between 3-5m, thus indicating a so called upside-down boundary layer. TKE values normally decrease in the vertical direction, because turbulence is more active at the surface. From the TKE records can be concluded that there is enhanced turbulence at 5m and 8m. Elevated turbulence is one of the upside-down boundary features described by Mahrt (1999) and is also related to drainage flows in a VSBL. Moreover, TKE decreases after passage of the head of the drainage flow.

The geographical relation between wind direction and drainage flow is visualised in figure 3.9. The drainage flow clearly originates from the higher area. However, the flow direction is more expected to be around 140 degrees considering the lowest point in the landscape. Note that the drainage flow might not follow a straight line and might eventually bend to the lowest area after passing the measurement station.

To summarize, interpretations of these observations are translated to a conceptual model of the shallow drainage flow showed in figure 3.10. The time lag of the 8m level suggests the micro-frontal shape of shallow drainage flow, however the evidence is not strong. Two vertical wind profiles are drawn, indicating the pulsating character of the wind speed. The dotted (blue) line and solid (red) line corresponds respectively with arrow 2 and 3 in figure 3.8. In the next sections, we will extent this model using more observations from the Divergence Site.

Temperature records

Previously, we showed that the vertical wind profile and wind direction are evidences of a typical shallow drainage flow. In this section we include an analysis of the temperature records showed in figure 3.11. Just before the passage of the drainage current, marked as point 1, the air temperature gradually increase ±2°C between 20:05 and 20:10 UTC. Temperature measurements at a fixed point cannot be used to examine the horizontal temperature structure. But given the wind direction (solid arrow in figure 3.9), it is likely that heat is advected from the relative warmer drainage gully after sunset. This is an clear example of the importance of small scale spatial heterogeneity in extreme stable conditions. Moreover, the temperature records show very complex behaviour with deviations of various time scales acting at the same time. Especially deviations characterized by a time scale ±1 minute are very remarkable. The corresponding ogive-wavelet of figure 3.5 indeed shows that most of the variance at 2m is caused by fluctuations between 1-3 min (reddish colors). It is not clear if the drainage flow itself caused this fluctuations.

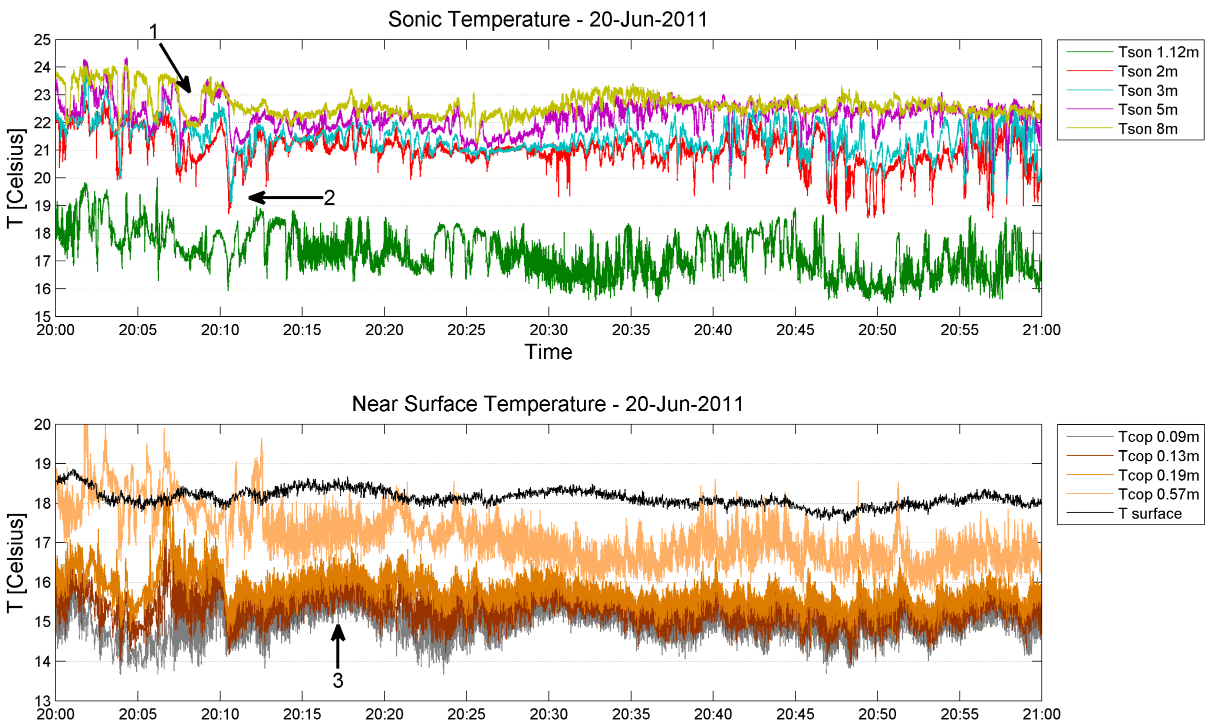

Figure 3.11: up) 20Hz Sonic Temperature of the Skinflow tower. down) 20Hz air temperature thermocouple data and 1Hz surface temperature data from the IR camera taken from the pixel where the tower was situated. Note that the absolute values are not comparable between the thermocouple temperature and sonic temperature.

Temperature suddenly drops around 3°C when the head of the drainage flow arrived the measurement station at point 2. The sudden drop does not occur above 5m. Hereafter, temperature values increase again. Such temperature drops are typical for drainage flows. Mahrt *et al.* (2010) reported a temperature drop of 2°C during drainage flow over a slope of 5.3°, however the decrease in temperature has continued for minutes. This head of the drainage flow acts as a cold microfront passage. A cold microfront of comparable depth was related to decreasing turbulence by Mahrt (2010). In contrast, figure 3.11 shows increasing near surface temperatures and a more turbulent signal. It must be noted that the study of Mahrt (2010) has no data <1m and might has missed the near surface turbulent activity. Here, it seems that air temperatures <0.57m and surface temperatures are affected by shear instability. Increasing shear lead to enhanced turbulence, mixing of air and thus a smaller temperature gradient. The temperature observations are added to our conceptual theory in figure 3.15 with cold air in front of the drainage flow head. Temperature profiles are added, which corresponds with arrow 2 (blue dotted) and 3 (red solid).

After 20:35 UTC, the drainage flow characteristics are less obvious. The 2m temperature shows only very large negative peaks, while 1m up records show predominantly positive peaks. Other levels does not show this clear interaction and this might be typical for the most accelerated level (2m).

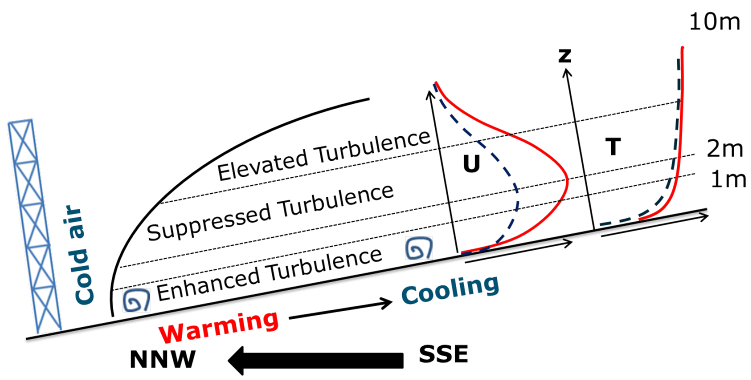

Figure 3.12: Schematic representation of the shallow drainage flow structure including the temperature observations.

Surface Temperature

Due to the high measurement frequency of surface temperature data, the analysis can be done by analysing a movie made of single frames. Six frames of surface temperatures at the measurement site are represented in figure 3.13. The buildings, pond and road are not interesting and did not receive a value. The water channel is clearly visible and much warmer than the surrounding surface. The records immediately shows substantial variations in space and time.

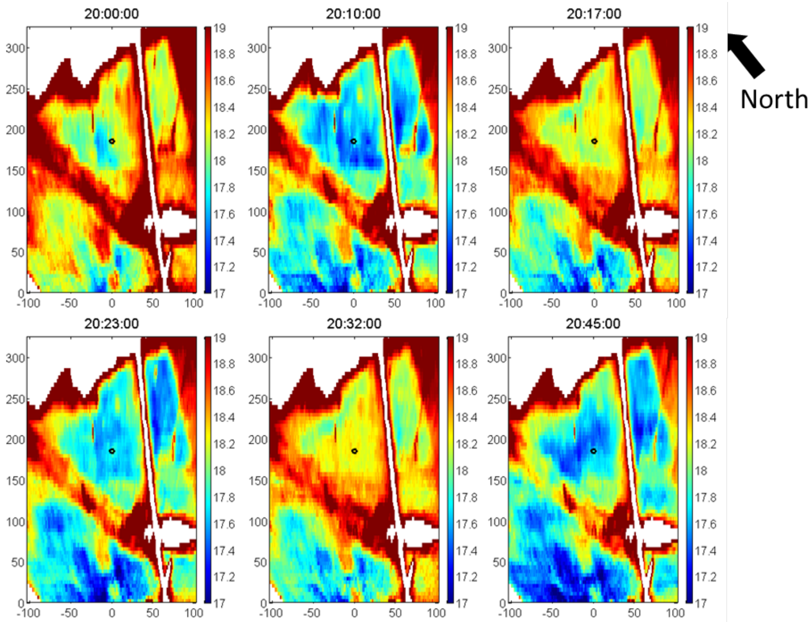

Figure 3.13: Six frames of surface temperatures at the divergence site. The location of the Skinflow Tower is black encircled and the white areas represents non-grass areas. Note that the box is not oriented to the North.

Surface temperature decreases between 20:00 and 20:10 UTC. The earlier noticed heat advection event at 20:05 UTC is not well visible in the surface temperature data. However, the surface temperature at the measurement station represented in figure 3.11 shows a slight increase in surface temperature. The surface temperature is relatively low as the drainage current arrives at the measurement site. In contrast to our expectation, the onset of the drainage current is characterized by increasing surface temperatures in stead of decreasing surface temperatures. The coldest spot vanishes in direction of the drainage flow. Earlier we note the enhanced turbulent activity and increased near surface temperatures induced by increased shear during the drainage flow pulse. Enhanced mixing might be a good explanation for the increasing surface temperatures. Surface temperature decreases again when the drainage flow decelerates between 20:17 and 20:23 UTC and the shear decreases. The surface temperature variation influenced by the drainage flow pulse is ± 0.6°C. Soler *et al.* (2002) reported a mixing event which causes a warming of 0.3°C in the 2cm subsoil layer. Taken into account the damping effect of the soil, the surface temperature warming should be sufficiently warmer than 0.3°C during that case. The use of IR photos in relation to drainage flows was not earlier reported in literature.

A new drainage flow cycle starts around 20:23 UTC and the same pattern happens as described above. The drainage flow continues after 20:32 UTC, but now shows more complex behaviour. The surface temperature gradually decreases until 20:48 UTC with ±0.6°C. The wind direction in figure 3.8 shows a small sudden shift in wind direction, typical for the next cycle. However, no clear wave cycles can be noticed from the wind speed records. The structures are too complex to extract relevant information from ordinary time series. It is even hard to extract relevant information from ordinary time series. Wavelet analysis gives relevant information about the time scales, but does not help to understand the flow.

Heat flux and vertical movement

Earlier, we showed that drainage flows affect the near surface turbulent activity and surface temperature. The vertical velocity and heat flux for 5 different levels are visible in figure 3.14. An exact value of heat flux is not necessary here, so the heat flux is simply approximated by multiplying $\overline{w'T'}$ by 1004 (C_p) and 1.2 (ρ). Moving averages are calculated from data around the current sample, which is useful for instantaneous fluxes.

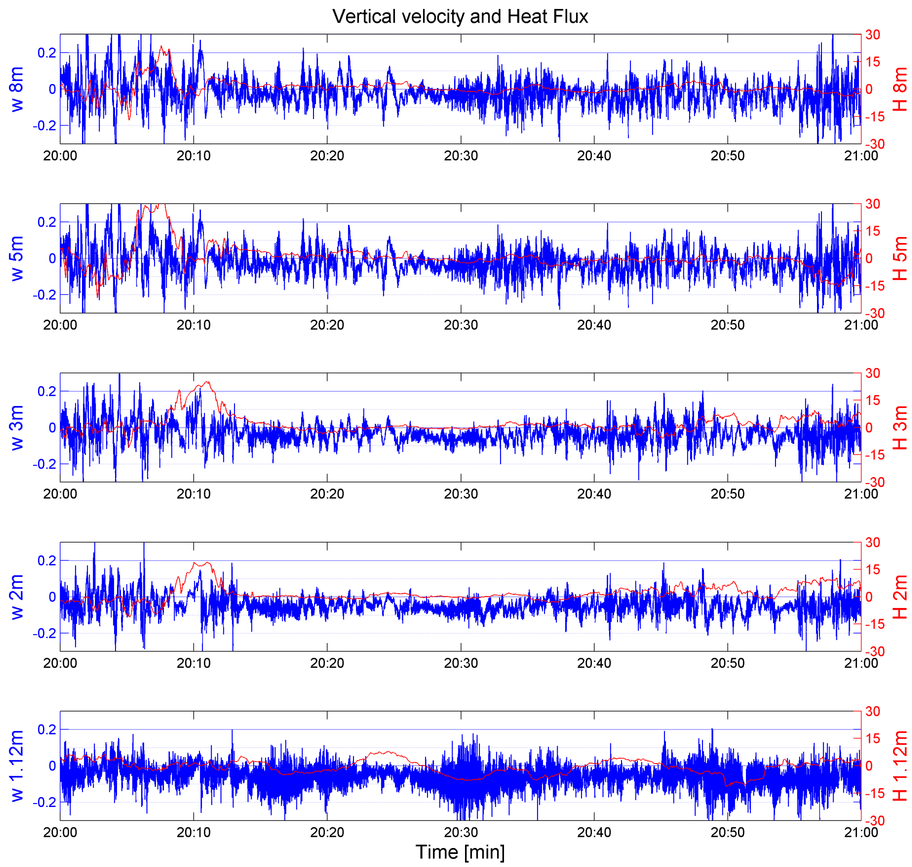

Figure 3.14: 20 Hz vertical velocity and 3 minutes moving average of heat flux from 5 levels of the EC skinflow tower. 3 minutes deviations of sonic temperature are used to calculate the turbulent heat flux.

The transported heat from the water channel is clearly captured in the heat fluxes in figure 3.14. The lag in the peak supports the explanation of increasing temperatures by advection. The warmer air parcels at higher levels firstly arrived the measurement station due to higher flow velocities, since the wind profile is still normal. The two earlier mentioned mixing events are visible in the w 1.12m record. However, the enhanced turbulence does not create a flux at the same time. In this case, turbulent mixing induced by drainage flow does only occur <1.12m.

A clear explanation for the disappeared wave cycles during the drainage flow is still not found in one of the time series. The signal of w seems a little more turbulent and the heat flux is slightly more positive/negative. This corresponds with the large temperature deviations between 1-2m starting from 20:30 UTC.

In theory, the cold air at the head of drainage flow is expected to creep underneath the warmer air layer. Hence, rising motions are expected at arrival of the shallow drainage flow. The vertical velocity records of figure 3.14 shows continuously rising and sinking motions prior to the arrival of the drainage flow head. Especially, the layer between 1.12-3m shows a rising motion with a duration of about 1-2 min. All levels show a transition to less vertical movements after the arrival of the drainage flow head at 20:10 UTC. Moreover, very typical rising and sinking osculations can be distinguished >2m after 20:20 UTC. These motions are related to the overturning eddies in the shallow drainage flow and are typical for wave-like phenomena. According to the magnitude of the vertical movements, these swirls of air are bigger on top of the shallow drainage flow. The interpretations of the vertical movements and overturning air are included in the theoretical concept of figure 3.15.

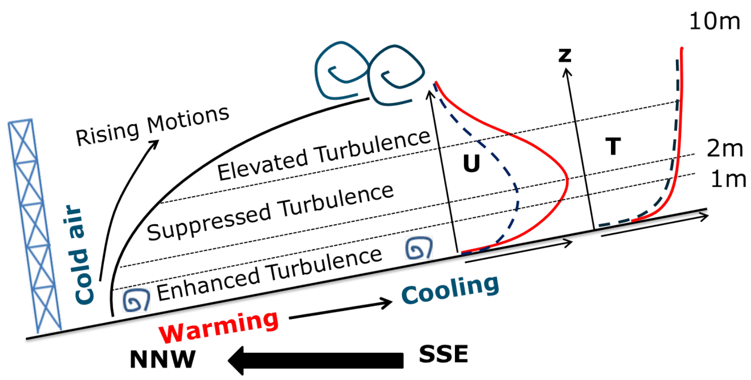

Figure 3.15: Schematic representation of the shallow drainage flow structure including the vertical motions.

TKE Budgets

TKE budgets are made according to the method described in chapter Materials and Methods. Again, we choose an average time of 3 minutes to calculate the shear, buoyancy, TKE tendency and dissipation terms in equation 2.7. Results can be found in figure 3.16 for three EC levels. The upper panel in the figure shows the TKE budgets terms in the late afternoon and early evening. Below, we zoom in on the period 19:00-21:00 UTC which includes the selected time frame of this case analysed in the previous sections.

From the upper plots of figure 3.16 can be concluded that the buoyancy term is very low compared to the shear term. Sensible heat fluxes <40 W/m^2 due to very low wind speeds caused these small buoyancy terms. Stationairity is often assumed when analysing TKE budgets, hence the TKE tendency is zero. Our analysis also supports this assumption. After 19:00 UTC, there is hardly any production nor destruction of TKE.

Unfortunately, the TKE budget analysis is not useful for this case and does add more physical understanding to this type of flow. Turbulent activity is located <1m according to the temperature records and thus outside the EC measurement locations. Turbulence >1m is too small to calculate significant budget terms. As a consequence, errors will have major impact on the budget terms and showing a very chaotic pattern. It is not possible to extract any relevant information with respect to the analysed drainage flow event between 20:00-21:00 UTC. In contrast, TKE budgets were found highly informative for the description of a shallow drainage flow over a steep Alpine slopes (Nadeau *et al.*, 2012).

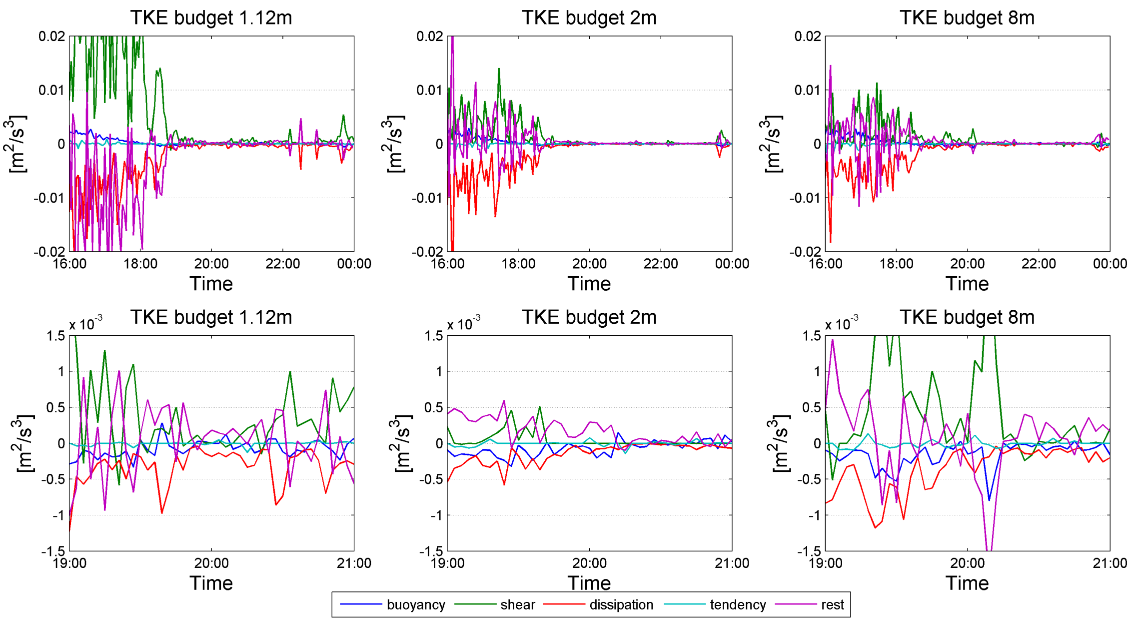

Figure 3.16: The upper panel shows 3 min averaged TKE budgets between 16:00-00:00 at 20-06. The lower pannel zooms shows a more detailed part between 19:00-21:00. Turbulence is elevated and mainly driven by shear.

3.4 Case 2: Drainage Flow 24-06

In this section we analyse the drainage flow event of 24-06, where we use the same structure as the previous section. Earlier presented 5 minute averaged vertical profiles in section 3.2 already showed evidence of an upside-down wind profile between 20:00-22:45 UTC. The next sections will concentrate on a small part within this time frame.

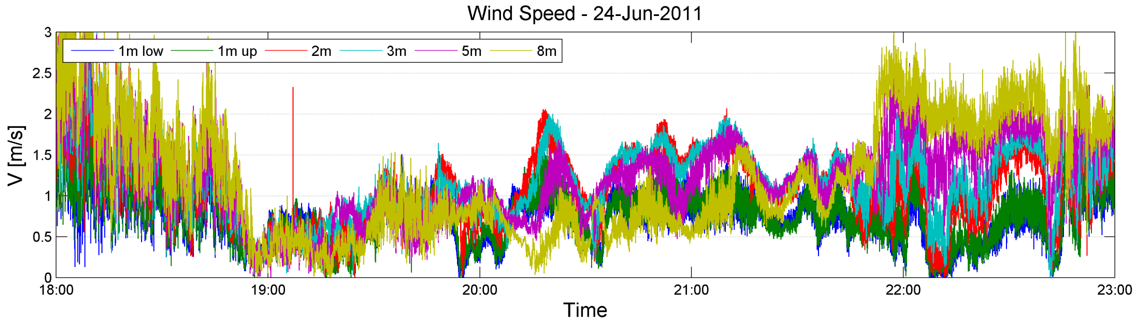

Figure 3.17: 20 Hz time series of wind speed from the 6 EC levels. Four clear shallow drainage flow pulses are visible with variable durations and clear lag between the various levels.

Drainage Flow Main Features

Figure 3.17 shows the high frequency EC data of the horizontal wind speed at six sonic levels. Extreme calm conditions are reached at 19:00 UTC where the flow is very close to 0 m/s. Hereafter, the boundary layer directly starts to decouple and the wind tends to deviate from its normal logarithmic wind profile. A clear shallow drainage flow develops around 20:00 UTC and continues till 21:45 UTC. The wind speed shows a wave-like pattern and the variance decreases. Four clear pulses are visible, where the length of the pulses ranges between 10 and 30 min. The time frame between 20:00-20:40 UTC is chosen for further analysis.

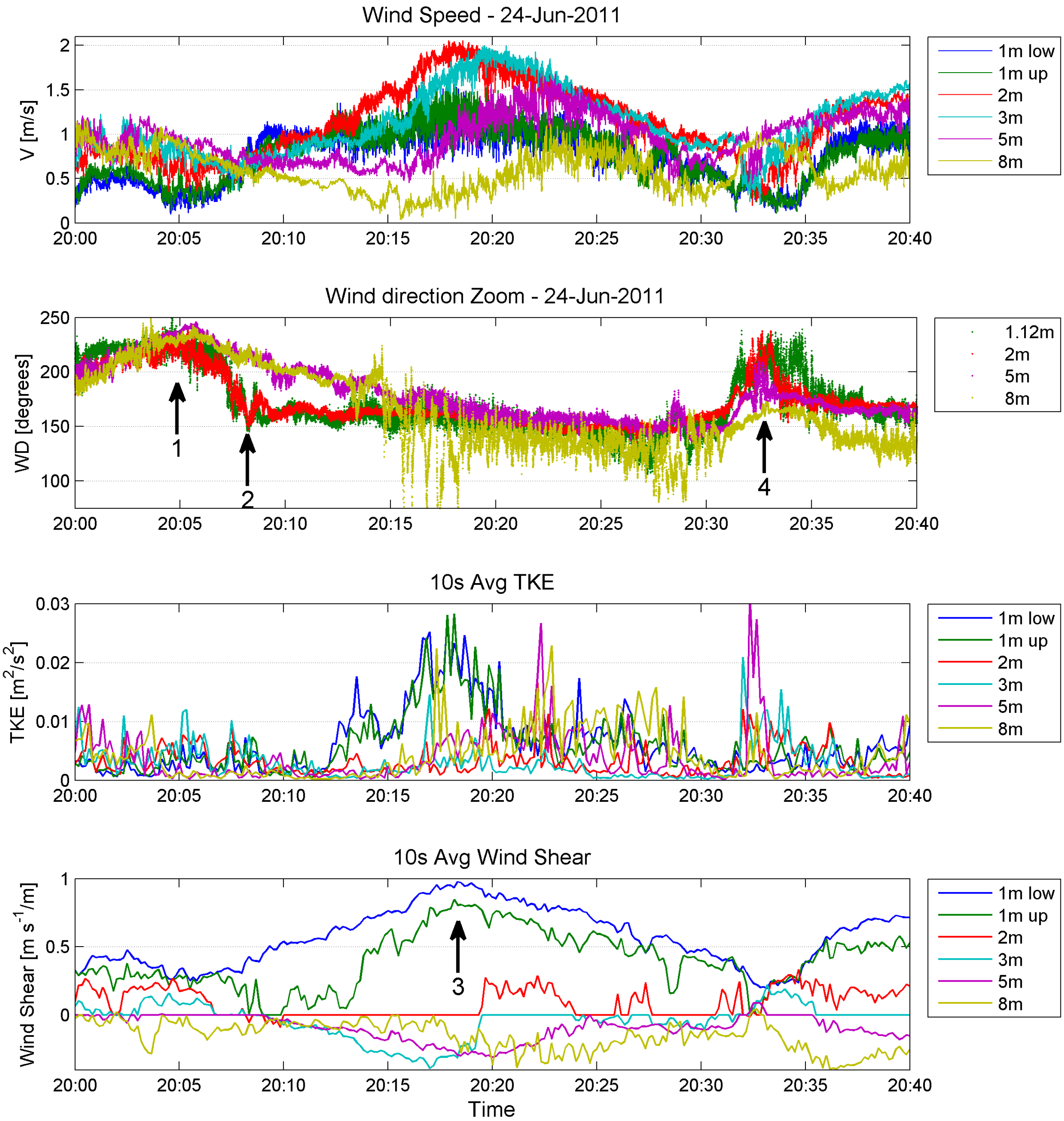

Figure 3.18: From up to down. 1) 20 Hz wind speed. 2) 20 Hz Wind direction. 3) TKE from 10 sec variances. 4) 10 sec averaged wind shear (wind gradient)

Similar to the previous case, 20 Hz time series of wind speed, wind direction, TKE and shear are shown in figure 3.18. Interesting points are indicated with an arrow and described later on. The most conspicuous features visible in figure 3.18 are the change in wind direction, upside-down wind profile and time lag of the maximum wind intensity. At point 1, backing of the wind direction starts and a change of ± 75 degrees occurred within three minutes considering the 1m and 2m levels. Backing of the wind direction between 5-8m is much slower, thus contributing to a decoupled situation. The relation between wind directions and the landscape is similar to the previous case as depicted earlier in figure 3.9.

We define the arrival of the drainage flow pulse at 20:05 UTC, indicated by point 1. From the wind speed series we can extract some information with respect to the shape of the flow. The 2m level shows the maximum wind speed within 10m. Considering this, the maximum jet is located around 2m. In order to calculate the lag between different layers, the wind speed signal is firstly smoothed by a 3 minute moving average. The lag is determined as $maxV_z - maxV_{2m}$, where z is one of the EC levels. Results can be found in table 3.1. Apparently, the pulse firstly arrived the Skinflow tower at the bottom two EC stations. Considering the time lag, the shape of this drainage flow pulse is similar to micro-front with a jet located around 2m. This observation supports the shallow drainage flow structure presented in the final conceptual flow model (figure 3.15 even more compared to the previous case.

Table 3.1: Time lag between the 2m level based on the maximum velocity peak

Level	**Lag [min]**
1m low	-0:44
1m up	-0:27
3m	+2:26
5m	+4:16
8m	+6:00

The TKE and wind shear graphs contributes to a situation with a decoupled boundary layer, where a clear distinction between the lowest two and the highest four levels is visible. Enhanced TKE is located at between 5-8m. The lower two levels show a positive shear, which refers to a normal wind profile. However, the shear between 2m and 8m is negative and thus deviate from a normal vertical profile. Maximum shear and TKE is reached at point 3, leading to less stability and the drainage flow starts to decelerate.

Temperature Records

In this section we show how the shallow drainage flow and surface heterogeneity affect the air and surface temperature represented in figure 3.19. The upper panel of figure 3.19 shows 6 sonic temperatures which are equal to the virtual temperature. It appeared that the 1m upper temperature signal has a large offset. It is chosen to include this record in the analysis, because the pattern still contains valuable information and absolute temperature values are of minor importance to describe the drainage flow. The bottom panel of the figure shows 4 thermocouples at the surface and the surface temperature from the IR camera.

The veering of the wind already started before 20:00 UTC and air temperatures are rising till point 1. The levels <5m starts to cool while the temperatures above continue rising. This can be explained by the surface heterogeneity and differences in wind directions between these layers. Warm air is still advected from wind direction ranging from approximately 200-240 degrees (SW). Before the start the drainage flow pulse, a large difference in temperature of $\pm 8.5°C$ exist in the first 8m. A bulb of cold air is passing the measurement station at point 2, which is also the end of shifting wind directions <5m. Then the flow starts to accelerate till point 3. Some interesting features can be distinguished between point 2 and 3:

- Surface temperature increases >1°C
- Decreasing temperatures between the jet and 0.57m, increasing temperature between surface and 0.57m.
- Enhanced turbulence.
- Large negative fluctuations at 2m.

The first near surface thermocouple at 9cm shows a temperature increase of almost 3°C. The increase in surface temperature is low compared to the near surface thermocouples. The IR camera has a resolution of 0.65m x 4.55m, whereas the thermocouples represents an area of a few centimetres. Hence, the surface temperature increase at the measurement station is more flattened out.

The temperature records suggest that the drainage flow triggers a kind mixing event <2m similar to the previous case. Large negative deviations can be determined from the 2m record, suggesting much interaction with the air below. Heat is transported downward, which might be a plausible explanation for the increasing near surface temperatures. The new drainage flow pulse arrives the measurement station at point 4 and is characterized by a cold air bulb passing the Skinflow Tower.

A very typical structure is marked as point 'a' between 20:25-20:30 UTC, when the back of the shallow drainage flow wave passes the measurement station. During this period, the 3m level does not correspond with the temperature structures of the layer below and above. Overturning motions are expected at the backside of drainage flows, which can explain the fluctuations due to transport of warm air from above and cold air from below. The question remains why the 3m level is not affected by the overturning air. Apparently, the large overturning eddies from above and below cannot break trough this layer.

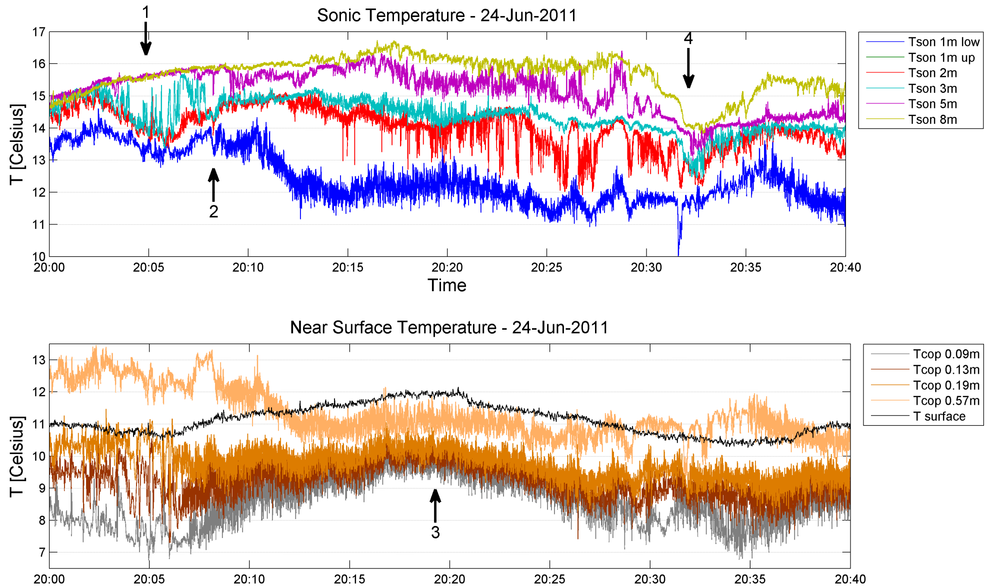

Figure 3.19: up) 20Hz Sonic Temperature of the Skinflow tower. Tson 1m up showed negative offset and is deleted. down) 20Hz air temperature thermocouple data and 1Hz surface temperature data from the IR camera taken from the pixel where the tower was situated. Note that the absolute values are not comparable between the thermocouple temperature and sonic temperature.

Surface Temperature

Again, six surface temperature frames are selected to illustrate the variations in surface temperature during the shallow drainage flow pulse. The coldest spot is located closely to lowest point in the field. The evolution of surface temperature in relation to the drainage is similar to what is described in the previous case. Subsequently figure 3.20 shows, a vanishing cold spot in direction of the drainage flow at point 1 to pint 3. Recreation of the cold spot also in direction of the flow from point 3 to point 4. The main differences compared to the previous case is the difference in absolute surface temperatures and the spatial variance of surface temperatures. The color scale of the previous case ranges between 17-19°C compared to 10-12°C presented here. The previous case also shows large cold spots south from the water channel, this part of the field is clearly warmer compared to the northern part in this case. Moreover, cooling and warming of the surface does not occur simultaneously at these different sites. A convincing explanation cannot be given, but it depicts the complexity, the fine scale of such phenomenon and the importance of local field heterogeneity.

Heat Flux and Vertical Movement

Previous sections suggest that the drainage flow triggers turbulent mixing close at the surface. Sensible heat flux H and vertical velocity w for the upper 5 EC levels are represented in figure

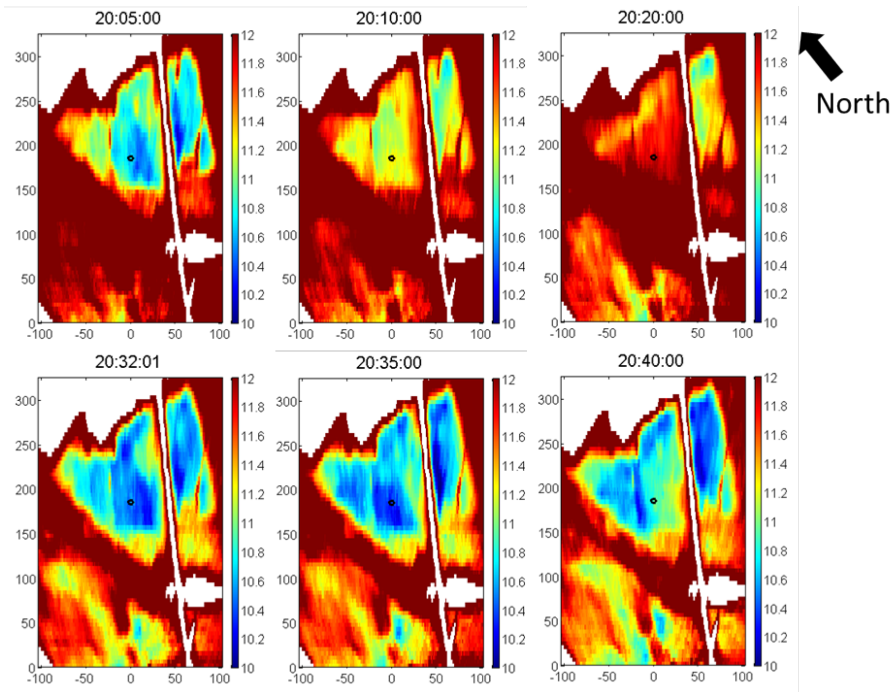

Figure 3.20: Six frames of surface temperatures at the divergence site, showing the pulsating behaviour as the wind field. The Skinflow Tower is represented by a black circle and the white areas are non-grass areas. Note that the box is not oriented to the north.

3.21 in order to receive more information about this mixing event. The drainage flow acts to some extent like a kind of micro-front as showed earlier. If so, the cold air will push the air upwards and is expected to be visible in the w records as depicted in a study of Viana *et al.* (2010).

Earlier, the arrival of the drainage flow pulse was estimated around 20:05 UTC mainly based on the turning wind direction. However, the pulse was not characterized by clear decreasing temperatures. Figure 3.21 shows upward motions around 19:55 UTC which suggest a cold air passage before the start of the drainage flow pulses. Further investigation of temperature records <20:00 UTC shows a temperature drop around 19:54 UTC, where the T_{2m} decreases from 15°C till 12°C. Afterwards, temperatures values recover to its original value. In contrast, figure 3.21 does show a change in vertical velocity signal as the second drainage flow pulse start at point 4. However a clear vertical movement cannot be distinguished. This drainage flow pulse is also characterized by a drop in temperature and a turning wind direction. Furthermore, the vertical velocity again depicts the elevated turbulence >3m.

In general, the sensible heat fluxes are very low (<10 W/m^2). Temperature records suggest interaction between the 2m level and air below around point 3, however evidence of this interaction cannot be found based on 3 minute averaged fluxes of H. The interaction probably takes place at a scale much smaller than 3 minutes and does not result in a net temperature change.

The minor warming of the 1m upper level due to the prospected mixing is too small to result in a measurable flux as well.

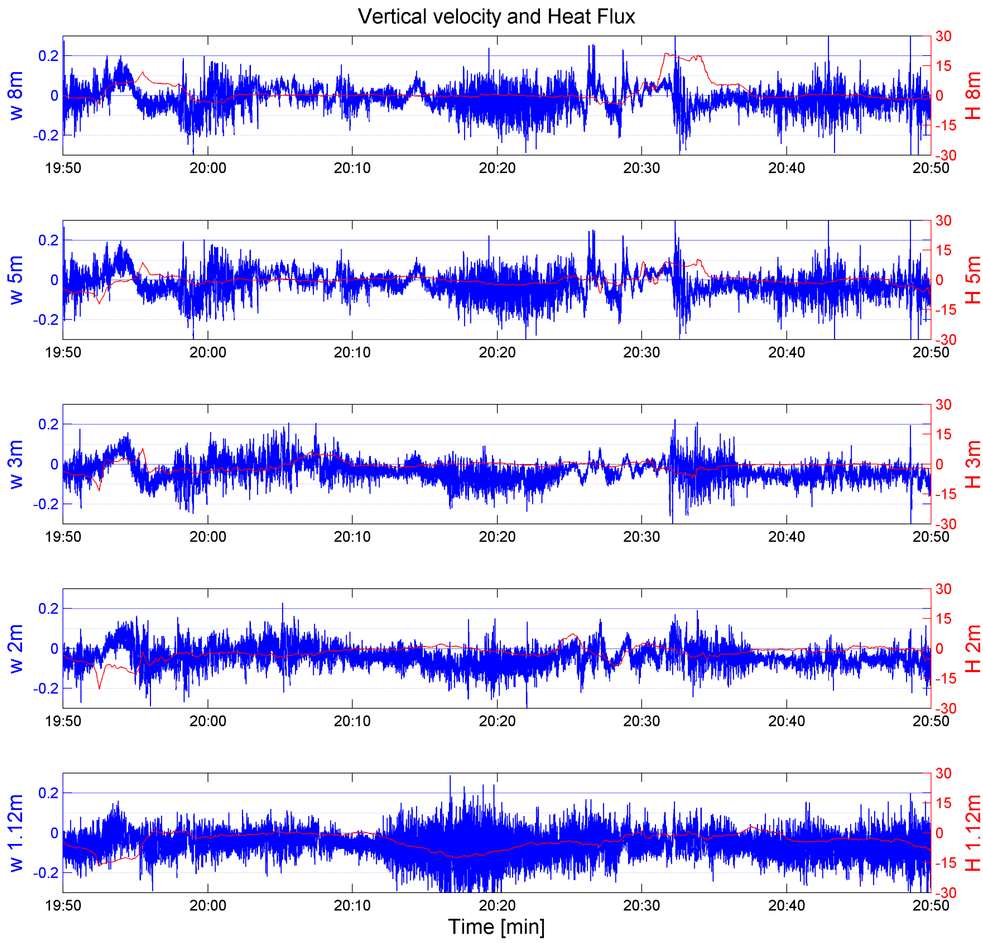

Figure 3.21: 20 Hz vertical velocity and 3 minutes moving average of heat flux from 5 levels of the EC skinflow tower. 3 minutes deviations of sonic temperature are used to calculate the turbulent heat flux.

TKE Budgets

TKE budgets were to some extent useless in the analysis of the previous case. The TKE budget results of this case are represented in figure 3.22, where only the 1m up, 2m and 8m EC levels are given. The early evening TKE conditions are very similar to the previous case with respect to the relation between the budget terms. Again, the buoyancy term is very low and shear decreases with height. Stationairity can be assumed, because the tendency is very low compared to the other terms. A detailed figure of the time span between 19:00-21:00 UTC is visible in the lower panel. The TKE budgets support the earlier noticed elevated turbulence by increasing budget terms with height. However, the time series of the TKE budget terms is still very chaotic. Pulses of TKE production by shear at 1m and 8m can be distinguished from the graphs and represents the two wave cycles between 20:00-21:00 UTC. At the jet maximum (2m) the derivative $\frac{dU}{dz}$ is approximately zero. Hence this method cannot detect turbulence by shear at the jet maximum, but evidence of turbulence at 2m is visible in the temperature records. The turbulence is on a very fine scale and there is no net change. Net change in TKE production/destruction by buoyancy probably takes place at levels <1m.

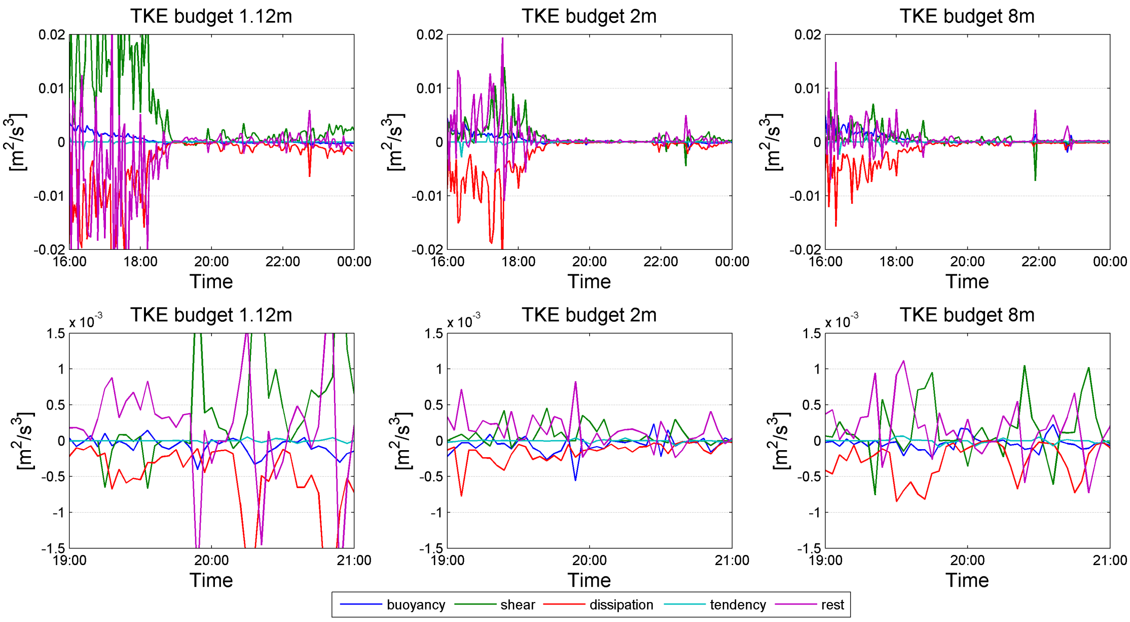

Figure 3.22: The upper panel shows TKE budget terms between 16:00-00:00 UTC on 24-06. There is hardly any production or destruction of TKE and the buoyancy term is very low. The lower panel zooms in on the shallow drainage flow event. Wavelike pattern is visible at 1.12m

3.5 Syntheses

During the analysis of the first case (20 June), a schematic sketch of the flow structure has been made based on the presented data analysis. The shallow drainage flow event on 24 June appeared to be generally similar to 20 June. Observations at 24 June supported the developed theoretical concept based on the observations at 20 June. Time series reveals clear oscillations in wind speed and near surface temperature in both cases. Observations at 24 June showed clear evidence of this micro-frontal shape, while observations at 20 June showed a more complex structure of the flow. Apart from the two described cases in this study, shallow drainage flow was also detected at the following less suitable cases, IOP 1(19-06), IOP 9 (01-07) and IOP 10 (02-07) by investigating 5min averaged vertical profiles.

Shallow drainage flow travels from SSE to NNW, which is in the same direction as the mesoscale katabatic flow direction. The katabatic flow continued after the dissipation of the upside-down wind profile within 10m. The depth of the flow is estimated around 10m, but there is no hard evidence due to missing data between 8 and 30m. A jet located between 8m and 30m might still be possible considering the corresponding flow direction. The question remains whether the stability is then large enough to decouple the air from surface friction forces. But given the directional wind shear between 8-30m this is not likely.

Chapter 4

Conclusions

In this thesis two extreme SBLs with a radiative SBL regime, characterized by a sensible heat flux around zero are studied. The aim of the study was to evaluate the fenology of near surface features in the radiative SBL. Low values of H, u^* and high values of z/L were found for IOP 3 (20-06) and IOP 4 (24-06) and therefore selected for further analysis. Mesoscale flows became important as consequence of weak synoptic forcing due to anticyclonic conditions on 20-06 and post-frontal conditions on 24-06. Averaging time of 5min appeared to be sufficient to detect upside-down wind profiles within 10m from the surface. Compared to ordinary wavelet analysis, the new developed ogive-wavelet method appeared to be more useful and easier to investigate small scale turbulence (<10 min) during the entire night in extreme stable conditions. The ogive-wavelet also supports the analysis of co-variances by using a co-wavelet. For each case we select a single time span just after the early evening calm period to evaluate the shallow drainage flow.

The arrival of drainage flows at the Skinflow tower was typically just after the early evening calm period during low wind conditions, when turbulence almost completely vanishes. There was no occurrence of drainage flow after midnight during the BLLAST campaign. The origin of the drainage flow could not be detected, because fixed point measurements were used. From the analysis can be concluded that the drainage flow often strengthen and weakens and follows an oscillatory pattern. Weakening of drainage flows occur when the shear instability exceeds a critical value. Onset of drainage flow pulses was often characterized by cold micro-fronts, which in turn are characterized by wind shifts up till 100 degrees and strong temperature drops. Influence of spatial heterogeneity became visible when wind shifts over warmer terrain and caused an advective heat flux of max 30 W/m^2. Wind shifts preferably occurred clockwise, but anti-clockwise shifts were also measured. TKE decay as well as TKE enhancement occurred at the arrival of new drainage flow pulses. Hence, a general pattern in TKE could not be detected. In both cases, the shape and depth of the drainage flow was approximately similar. The maximum jet was located between 2-3m, where the maximum velocity of 2 m/s seemed to be a critical value. The upper level was clearly lagging compared with the levels below, which indicates the micro-frontal shape of drainage flows.

Temperature records from the EC skinflow tower showed very complex structures. At the maximum jet (2m), very fast and large negative temperature deviations were present. However, these deviations did not cause a net change in temperature. Increased shear instability caused by the drainage flow oscillations appeared to be the main drive of turbulent mixing <2m. The turbulent mixing caused near surface warming up till 3 °C at 9cm. Less surface warming was measured by the IR camera, but these values are hard to compare due to a different measurement technique and a much larger representative measurement area (few cm^2 compared to m^2). Results of the IR-camera showed that the surface warming and cooling oscillations induced by drainage flows are site-specific within the measurement site. Studying the physics of shallow drainage flow appeared to be challenging due to very flow fluxes. Contribution of TKE budget analysis to the understanding of shallow drainage flow was minimal, because the most turbulent activity was below the EC levels.

The presence of shallow drainage flow might be taken into account in future BLLAST studies, especially when fluxes are part of the analysis. Structures are very complex and researchers can take advantage by knowing the presence of upside-down SBLs by forehand.

Recommendations

It can be concluded that the BLLAST measurement site is suitable to study shallow drainage flow. Some changes in the experimental design may help in a better understanding of such submeso flows. The present study failed in quantifying the speed of the drainage flow. A triangular set-up of EC towers in future experiments at this site might contribute to more insight in the flow structures and velocities of the system. Moreover, this study showed clear evidence of turbulent processes <1-2m. The Skinflow tower was equipped with small path length sonic anemometers at 0.85m and 1.12m. However, this study to some extent failed to examine TKE budgets due to measurement failure of the lowest level and turbulent mixing predominantly <1m. It is advised to mount additional small path length sonic anemometers <0.5m in future experiments.

Moreover, the present study can be extended by using additional data from the BLLAST campaign. Here, we only used 5min averaged EC-pack output from the 60m Valimev tower. The question remains whether the sudden temperature drops and wind shift related to the micro-fronts are still noticeable at elevations higher than 8m. Investigating of the raw data may answer this question. No effort has been made to study the shallow drainage flow dissipation. Figures like 3.3 and 3.4 indicate a relation with the upper air velocity field. The BLLAST dataset is very suitable to study this dissipation mechanism. Also, there is still work left to compare the observational data with existing mathematical descriptions and models of drainage flows.

Acknowledgements

This thesis is part of my MSc in Earth and Environment and carried out at the Meteorology and Air Quality (MAQ) department of Wageningen University under supervision of Oscar Hartogensis. I would like to thank Oscar for providing and developing of a lot of Matlab code and the discussions during my MSc Thesis. Moreover, I would like to thank Anirban Garai from the University of California for his quick response and preparation of the IR camera dataset.

References

2011. *BLLAST 2011 Experimental Plans*. Tech. rept. Observatoire Midi-Pyrenees.

Acevedo, O., Costa, F., Oliveira, P., Puhales, F., Degrazia, G., & Roberti, D. 2013. The influence of submeso processes on stable boundary layer similarity relationships. *J. Atmos. Sci.* in press.

Baas, P., Steeneveld, G.J., van de Wiel, B.J.H., & Holstlag, A.A.M. 2006. Exploring self-correlation in flux-gradient relationships for stably stratified conditions. *Journal of the Atmospheric Sciences*, **63**(11), 3045–3054. cited By (since 1996) 35.

Brazel, A. J., Fernando, H. J. S., Hunt, J. C. R., Selover, N., Hedquist, B. C., & Pardyjak, E. 2005. Evening transition observations in Phoenix, Arizona. *Journal of Applied Meteorology*, **44**(1), 99–112. Cited By (since 1996):21.

De Coster, O.M.Y., & Pietersen, H.P. 2011. *BLLAST- uniform processing of Eddy-Covariance data*. Tech. rept. Wageningen University. Student Report.

De Moortel, I., Munday, S.A., & Hood, A.W. 2004. Wavelet Analysis: the effect of varying basic wavelet parameters. *Solar Physics*, **222**(2), 203–228.

Hartogensis, O.K., De Bruin, H.A.R., & Van De Wiel, B.J.H. 2002. Displaced-Beam Small Aperture Scintillometer Test. Part Ii: Cases-99 Stable Boundary-Layer Experiment. *Boundary-Layer Meteorology*, **105**(1), 149–176.

Howell, J.F., & Sun, J. 1999. Surface-layer fluxes in stable conditions. *Boundary-Layer Meteorology*, **90**(3), 495–520. cited By (since 1996) 82.

Kumar, Praveen, & Foufoula-Georgiou, Efi. 1997. Wavelet analysis for geophysical applications. *Reviews of Geophysics*, **35**(4), 385–412.

Mahrt, L. 1999. Stratified Atmospheric Boundary Layers. *Boundary-Layer Meteorology*, **90**, 375–396.

Mahrt, L. 2010. Common microfronts and other solitary events in the nocturnal boundary layer. *Quarterly Journal of the Royal Meteorological Society*, **136**(652), 1712–1722.

Mahrt, L., & Vickers, D. 2006. Extremely weak mixing in stable conditions. *Boundary-Layer Meteorology*, **119**(1), 19–39. cited By (since 1996) 55.

Mahrt, L., Vickers, D., Nakamura, R., Soler, M.R., Sun, J., Burns, S., & Lenschow, D.H. 2001. Shallow drainage flows. *Boundary-Layer Meteorology*, **101**(2), 243–260. cited By (since 1996) 79.

Mahrt, L., Thomas, C.K., & Prueger, J.H. 2009. Space-time structure of mesoscale motions in the stable boundary layer. *Quarterly Journal of the Royal Meteorological Society*, **135**(638), 67–75. cited By (since 1996)9.

Mahrt, L., Richardson, S., Seaman, N., & Stauffer, D. 2010. Non-stationary drainage flows and motions in the cold pool. *Tellus, Series A: Dynamic Meteorology and Oceanography*, **62**(5), 698–705. cited By (since 1996)5.

Mahrt, Larry. 2009. Characteristics of Submeso Winds in the Stable Boundary Layer. *Boundary-Layer Meteorology*, **130**(1), 1–14.

Mahrt, Larry, Thomas, Christoph, Richardson, Scott, Seaman, Nelson, Stauffer, David, & Zeeman, Matthias. 2013. Non-stationary Generation of Weak Turbulence for Very Stable and Weak-Wind Conditions. *Boundary-Layer Meteorology*, **147**(2), 179–199.

Monti, P., Fernando, H. J. S., Princevac, M., Chan, W. C., Kowalewski, T. A., & Pardyjak, E. R. 2002. Observations of flow and turbulence in the nocturnal boundary layer over a slope. *Journal of the Atmospheric Sciences*, **59**(17), 2513–2534. Cited By (since 1996):96.

Nadeau, Daniel F., Pardyjak, Eric R., Higgins, Chad W., Huwald, Hendrik, & Parlange, Marc B. 2012. Flow during the evening transition over steep Alpine slopes. *Quarterly Journal of the Royal Meteorological Society*, n/a–n/a.

Nadeau, DanielF., Pardyjak, EricR., Higgins, ChadW., Fernando, HarindaJosephS., & Parlange, MarcB. 2011. A Simple Model for the Afternoon and Early Evening Decay of Convective Turbulence Over Different Land Surfaces. *Boundary-Layer Meteorology*, **141**(2), 301–324.

Oncley, S.P., Friehe, C.A., Larue, J.C., Businger, J.A., Itsweire, E.C., & Chang, S.S. 1996. Surface-layer fluxes, profiles, and turbulence measurements over uniform terrain under near-neutral conditions. *Journal of the Atmospheric Sciences*, **53**(7), 1029–1044. cited By (since 1996)85.

Pino, D., & Villa, J. 2011. *IOP summary*. Tech. rept.

Seaman, N.L., Gaudet, B.J., Stauffer, D.R., Mahrt, L., Richardson, S.J., Zielonka, J.R., & Wyngaard, J.C. 2012. Numerical prediction of submesoscale flow in the nocturnal stable boundary layer over complex terrain. *Monthly Weather Review*, **140**(3), 956–977. cited By (since 1996) 1.

Soler, M.R., Infante, C., Buenestado, P., & Mahrt, L. 2002. Observations of nocturnal drainage flow in a shallow gully. *Boundary-Layer Meteorology*, **105**(2), 253–273. cited By (since 1996) 30.

Sorbjan, Z., & Grachev, A.A. 2010. An evaluation of the flux-gradient relationship in the stable boundary layer. *Boundary-Layer Meteorology*, **135**(3), 385–405. cited By (since 1996) 9.

Steeneveld, Gert-Jan, Nappo, CarmenJ., & Holtslag, AlbertA.M. 2009. Estimation of orographically induced wave drag in the stable boundary layer during the CASES-99 experimental campaign. *Acta Geophysica*, **57**(4), 857–881.

Stull, R.B. 1988. *An Introduction to Boundary Layer Meteorology*. 4 edn. Springer Science.

Sun, Jielun, Burns, SeanP., Lenschow, DonaldH., Banta, Robert, Newsom, Rob, Coulter, Richard, Frasier, Stephen, Ince, Turker, Nappo, Carmen, Cuxart, Joan, Blumen, William, Lee, Xuhui, & Hu, Xin-Zhang. 2002. Intermittent Turbulence Associated with a Density Current Passage in the Stable Boundary Layer. *Boundary-Layer Meteorology*, **105**(2), 199–219.

Torrence, C., & Compo, G.P. 1998. A Practical Guide to Wavelet Analysis. *Bulletin of the American Meteorological Society*, **79**(1), 61–78. cited By (since 1996)3325.

Van de Wiel, B. 2002. *Intermittent turbulence and oscillations in the stable boundary layer over land*. PhD Thesis, Wageningen University.

Van de Wiel, B.J.H., Moene, A.F., Hartogensis, O.K., De Bruin, H.A.R., & Holtslag, A.A.M. 2003. Intermittent turbulence in the stable boundary layer over land. Part III: A classification for observations during CASES-99. *Journal of the Atmospheric Sciences*, **60**(20), 2509–2522. cited By (since 1996) 48.

van Dijk, A., Moene, A.F., & Bruin, H.A.R. De. 2004. *The principles of surface flux physics: theory, practice and description of the ECPACK library*. Internal report. Wageningen University.

Van Kesteren, Bram. 2012. *Measuring water-vapour and carbon-dioxide fluxes at field scales with scintillometry*. PhD Thesis, Wageningen University.

Viana, S., Terradellas, E., & Yagüe, C. 2010. Analysis of gravity waves generated at the top of a drainage flow. *Journal of the Atmospheric Sciences*, **67**(12), 3949–3966. cited By (since 1996)5.

Wilczak, JamesM., Oncley, StevenP., & Stage, StevenA. 2001. Sonic Anemometer Tilt Correction Algorithms. *Boundary-Layer Meteorology*, **99**(1), 127–150.